

Erosion rates in a wet, temperate climate derived from rock luminescence techniques

Rachel K. Smedley¹, David Small², Richard S. Jones^{2,3}, Stephen Brough¹, Jennifer Bradley¹, Geraint T.H. Jenkins⁴

¹ School of Environmental Sciences, University of Liverpool, Liverpool, UK.

² Department of Geography, Durham University, South Road, Durham, UK.

³ School of Earth, Atmosphere and Environment, Monash University, Melbourne, Australia.

⁴ Independent researcher: Powys, Wales, UK

Correspondence to: Rachel K. Smedley (rachel.smedley@liverpool.ac.uk)

Abstract

A new luminescence erosion-meter has huge potential for inferring erosion rates on sub-millennial scales for both steady and transient states of erosion, which is not currently ~~not~~ possible with any existing techniques capable of measuring erosion. This study applies new rock luminescence techniques to a well-constrained scenario provided by the Beinn Alligin rock avalanche, NW Scotland. Boulders in this deposit are lithologically consistent, have known cosmogenic nuclide ages, and independently-derived Holocene erosion rates. We find that luminescence-derived exposure ages for the Beinn Alligin rock avalanche were an order of magnitude younger than existing cosmogenic nuclide exposure ages, suggestive of high erosion rates (as supported by field evidence of quartz grain protrusions on the rock surfaces). Erosion rates determined by luminescence were consistent with independently-derived rates measured from boulder-edge roundness. Inversion modelling indicates a transient state of erosion reflecting the stochastic nature of erosional processes over the last ~4.5 ka in the wet, temperate climate of NW Scotland. Erosion was likely modulated by known fluctuations in moisture availability, and to a lesser extent temperature, which controlled the extent of chemical weathering of these highly-lithified rocks prior to erosion. The use of a multi-elevated temperature, post-infra-red, infra-red stimulated luminescence (MET-pIRIR) protocol (50, 150 and 225°C) was advantageous as it identified samples with complexities introduced by within-sample variability (e.g. surficial coatings). This study demonstrates that the luminescence erosion-meter can infer accurate erosion rates on sub-millennial scales and identify transient states of erosion (i.e. stochastic processes) in agreement with independently-derived erosion rates for the same deposit.

1. Introduction

Rock erosion is dependent upon a variety of internal (e.g. mineralogy, grainsize, porosity, structures) and external (e.g. temperature, moisture availability, snow cover, wind, aspect) factors. Chemical and/or physical weathering of rocks (or rock

31 decay; Hall et al. 2012) breaks down the surficial materials making them available for transportation (i.e. erosion), where the
32 rates and processes of degradation is primarily controlled by the rock lithology (e.g. Twidale, 1982; Ford and Williams,
33 1989). For boulders with similar lithologies, the erosion rate is conditioned by weathering principally caused by moisture
34 availability, but also temperature, and in some cases biological factors (Hall et al. 2012). It is widely reported that warmer
35 temperatures increase most rates of chemical activity, while sub-zero temperatures arrest chemical activity on a seasonal
36 basis. However, cold temperatures alone do not preclude chemical weathering (Thorn et al. 2001). As such, rock erosion
37 rates will be sensitive to changing climate (moisture availability, temperature) such as that experienced throughout the Late
38 Holocene (i.e. last 4 ka) (e.g. Charman, 2010), in addition to that forecast for the future due to anthropogenic climate change
39 (e.g. Stocker et al. 2013).

40 Measuring erosion rates over shorter ($\leq 10^3$ a) and longer ($\geq 10^4$ a) integration times is advantageous as each targets a different
41 phenomenon of erosion. Longer timeframes will inform on how landscapes respond to changing large-scale climatic and
42 tectonic conditions (e.g. Herman et al. 2010), whereas shorter timeframes assess local or regional responses to shorter-lived
43 environmental conditions (e.g. climate fluctuations). A number of techniques can constrain long-term, landscape erosion
44 rates on $\geq 10^4$ a timeframes, such as cosmogenic nuclides (e.g. Lal, 1991; Braun et al. 2006; Balco et al. 2008) or
45 thermochronology (Reiners and Brandon, 2006). While observational measurements on very short timeframes $\leq 10^2$ a are
46 performed with both direct contact (e.g. Hanna, 1966; High and Hanna, 1970; Trudgill et al. 1989) and non-contact (e.g.
47 Swantesson, 1989; Swantesson et al. 2006) techniques. However, until now it has been difficult to constrain erosion rates on
48 10^2 to 10^3 a timeframes due to a lack of techniques with the required sensitivity and resolution.

49 The luminescence signal within mineral grains (quartz and feldspar) is reset when a rock surface is exposed to
50 sunlight for the first time (e.g. Habermann et al. 2000; Polikreti et al. 2002; Vafiadou et al. 2007). With continued exposure
51 the luminescence signal resetting in the mineral grains propagates to increasing depths (i.e. the luminescence depth profile is
52 a function of time). Improved understanding of this fundamental principle has led to the development of new applications of
53 luminescence; constraining the timing of rock exposure events (Laskaris and Liritzis, 2011; Sohbaty et al. 2011; Lehmann et
54 al. 2018) and rock surface erosion rates (Sohbaty et al. 2018; Lehmann et al. 2019a,b). Brown (2020) even combine these
55 phenomena within model simulations to explore different sample histories of exposure and burial, to inform
56 geomorphological interpretations of luminescence depth profiles measured for samples collected from the natural
57 environment. Here, we ~~measure~~ investigate erosion rates, rather than weathering rates as the luminescence technique
58 specifically measures the light penetration into a rock surface after the removal of material (i.e. erosion), occurring after the
59 in-situ rock breakdown (i.e. weathering). Luminescence depth profiles are a product of the competing effects of time (which
60 allows the bleaching front to propagate to greater depths) and erosion (which exhumes the bleaching front closer to the
61 surface). Existing studies have suggested that rock luminescence exposure dating is only feasible for very short timeframes
62 (e.g. < 300 a; Sohbaty et al. 2018) as light penetrates faster than the material can be removed, and/or in settings where erosion
63 rates are < 1 mm/ka (Lehmann et al. 2018). Beyond this, the dominant control on the luminescence depth profile is erosion,

rather than time, hence if time can be parameterised, then erosion can be determined (and vice versa). [Recent findings from erosion simulations compared with measured data have shown that the erosion rates derived from luminescence depth profiles can be accurate even where stochastic erosion was experienced in nature \(Brown and Moon, 2019\).](#)

New luminescence techniques have the potential to derive 10^2 to 10^3 a scale erosion rates because of two important characteristics: (1) measurable luminescence depth profiles can develop in a rock surface over extremely short durations of sunlight exposure (e.g. days; Polikreti et al. 2003, or years; Lehmann et al. 2018); and (2) luminescence depth profiles are sensitive to mm-scale erosion. Conversely, cosmogenic nuclides are sensitive to m-scale erosion, depending on the density (e.g. Lal, 1991). Therefore, the new luminescence erosion-meter has the potential to provide a step-change in capabilities of measuring erosion rates on currently impossible 10^2 to 10^3 a timeframes. However, its application has been limited to few studies (e.g. Sohbaty et al. 2018; Lehmann et al. 2019b) validated against long-term erosion rates of landscape evolution from global or regional datasets rather than local, independently-constrained erosion rates derived from the same rock type.

This study tests the accuracy and applicability of rock erosion rates inferred from luminescence techniques in a new latitudinal (57°N) and climate (wet, temperate) setting with independently-constrained erosion rates. The Beinn Alligin rock avalanche in NW Scotland (Fig. 1) provides a well-constrained test scenario as: (1) the boulders were sourced from a single fault-bounded failure scarp occurring within sandstones of the Torridonian group (i.e. rocks are likely to be lithologically consistent); (2) all boulder samples share an identical exposure history as they were deposited by a single, instantaneous event ([Ballantyne and Stone, 2004](#)); (3) independent cosmogenic exposure ages constrain the timing of the rock avalanche (Ballantyne and Stone, 2004); and (4) independently-derived erosion rates over the last ~ 4 ka for the boulders of the Beinn Alligin rock avalanche uniquely provide constraints on erosion rates (Kirkbride and Bell, 2010).

2. Theoretical background

The propagation of a bleaching front (i.e. the depth at which the luminescence signal has been reduced by 50 %) into a rock surface can be described by a double exponential function (Eq. 1), where L_x is the luminescence measured with depth (x) from the rock surface, L_0 is the saturation limit for this sample (determined experimentally), t is the exposure time, $\overline{\sigma\phi_0}$ is the intensity of light of a specific wavelength at the rock surface, and μ is the light attenuation coefficient. To determine the exposure time (t) of a rock surface ([and also erosion rates](#)), it is necessary to parameterise μ and $\overline{\sigma\phi_0}$, which are likely unique to any specific rock lithology and natural sunlight conditions (e.g. latitude, cloudiness) of the sample being dated, respectively. Therefore, to provide accurate luminescence exposure ages ([and also](#) erosion rates), μ and $\overline{\sigma\phi_0}$ must be calibrated using samples of known-age with the same lithology and natural sunlight conditions (e.g. a nearby road-cutting).

$$L_x = L_0 e^{-\overline{\sigma\phi_0}t} e^{-\mu x} \quad (1)$$

Studies have applied rock luminescence techniques (mostly exposure dating) to a variety of lithologies including granites, gneisses (Lehmann et al. 2018, 2019a,b; Meyer et al. 2019), sandstones (Sohbaty et al. 2012; Chapot et al. 2012; Pederson et al. 2014), ~~and~~ quartzites (Glignani et al. 2019) [and carbonate limestone \(Brill et al. 2021\)](#). These studies showed that μ is highly dependent upon the rock lithology, where mineralogy has a strong control on the rock transparency. This is supported

97 by direct measurements of μ for a variety of lithologies (greywacke, sandstone, granite, and quartzite) using a spectrometer
98 (Ou et al. 2018). In addition to mineralogy, it has also been shown that the precipitation of dark Fe-hydroxides (Meyer et al.
99 2018) and rock varnishing (or weathering crusts) (e.g. Luo et al. 2019) can influence μ by changing the rock transparency
100 principally at the rock surface. Mineralogy is broadly a constant variable over time. However, the formation of precipitates
101 or rock varnishing can be time-variable due to changing environmental factors external to the rock; thus, we ~~must~~should
102 consider the possibility that μ may be time-variable. Consequently, investigating the rock opacity of each sample is
103 important to assess whether the known-age samples used to parameterise μ and $\overline{\sigma\varphi_0}$ were consistent with the unknown-age
104 samples used for exposure dating or erosion rates.

105 Since the introduction of the new rock luminescence techniques, most studies on K-feldspar (except Luo et al.
106 2019) have only utilised the IR₅₀ signal as it bleaches more efficiently with depth into rock surfaces compared to higher
107 temperature post-IR IRSL signals (e.g. Luo et al. 2019; Ou et al. 2018). However, electron multiplying charged coupled
108 device (EMCCD) measurements of four rock types (quartzite, orthoclase and two different granites) have shown that the
109 post-IR IRSL signals of rock slices were dominated by K-feldspars, while Na-rich feldspars can contribute towards the IR₅₀
110 signal (Thomsen et al. 2018). It is possible that the different IRSL signals will have different luminescence characteristics
111 (e.g. bleaching rates, fading rates, saturation levels, light attenuation, internal mineral composition) that could be exploited
112 during measurements. Luo et al. (2019) used the post-IR IRSL signals with a multiple elevated temperature (MET) protocol
113 (50, 110, 170, 225 °C) to demonstrate that all the IRSL signals provide luminescence depth profiles, but the lower
114 temperature signals penetrated further into the rock with depth. The authors fit the four IRSL signals to improve the accuracy
115 of their parameterisation of μ and $\overline{\sigma\varphi_0}$. However, no study has yet used the MET-post IR IRSL protocol to exploit the
116 differing luminescence characteristics of the simultaneously~~successively~~-measured IRSL signals to provide an internal
117 quality control check on the reliability of the measured data, i.e. the luminescence depth profile will penetrate deeper in to
118 the rock for the IR₅₀ signal than the pIRIR₁₅₀ signal, which in turn will penetrate deeper than the pIRIR₂₂₅ signal. However,
119 all three signals should determine the same erosion rates if the model parameterisation (i.e. μ and $\overline{\sigma\varphi_0}$) is accurate. To
120 maximise the potential information that could be derived from the samples, this study applied a MET-post IR IRSL protocol
121 (50, 150 and 225 °C).

122 For determining erosion rates for rock surfaces of known exposure age, Sohbaty et al. (2018) used a confluent
123 hypergeometric function to provide an analytical solution, but assuming only steady-state erosion. Lehmann et al. (2019a)
124 provide a numerical approach that exploits the differential sensitivities to erosion of the luminescence (short-term) and
125 cosmogenic nuclide (longer-term) techniques to erosion to infer erosion histories (steady state and transient over time) for
126 rock surfaces. ~~By applying a step function from zero to increased constant erosion rates at certain times in history, This~~
127 approach uses the experimental data from the luminescence depth profiles and the ¹⁰Be concentrations for each sample.
128 Modelling of the luminescence depth profiles accounts for the electron trapping dependent upon the environmental dose-rate
129 and D₀ but does not consider athermal loss of the signal (i.e. anomalous fading) as it has been demonstrated to have a

negligible impact upon the luminescence depth profiles (Lehmann et al. 2019a). Modelling of the ^{10}Be concentrations assumes that no inheritance of the cosmogenic nuclides from prior exposure has occurred, and that the ^{10}Be concentrations have been corrected for the sample depth, sample and density and topographical shielding, local production rates, and the sample location (longitude, latitude and elevation). The combined experimental data for the luminescence depth profiles and cosmogenic nuclide concentrations are solved simultaneously for two unknowns: the exposure age and the erosion rate history as defined by a step function (e.g. zero erosion for an initial period of time followed by an instant increase to a constant erosion rate). Forward modelling is used to calculate all of the possible combinations of luminescence depth profiles and ^{10}Be concentrations for these synthetic erosion and exposure histories, which are then validated using inversion models against the experimental data to determine the combinations with the highest likelihood. A forbidden zone is defined where the range of possible solutions combinations of erosion rates and durations that are in excess of those that are feasible not possible given for the experimental measured ^{10}Be concentrations provided for the sample; these solutions are excluded from the parameter ranges used for the inversion model. For example, the forbidden zone identified in the inversion model profile shown in Fig. 7A is restricted to ranges from ca. 10^4 mm/ka for durations of ca. 100 a to ca. 10^3 mm/ka for ca. >3000 a.

The approach of Lehmann et al. (2019a) can model synthetic erosion histories in both steady and transient states. Steady state erosion is defined as a constant erosion rate over a portion of throughout the duration total duration of surface exposure. Transient erosion is typical of shorter exposure histories where a steady state of erosion has not yet been reached and is defined by erosion rates that decrease linearly with increased timing of erosion onset within the parameter space. Transient erosion varies with time and was simulated here by assuming that the evolution of erosion in time follows a stepped function of a fixed increase in erosion rate from zero for varying durations throughout the exposure history for each synthetic erosion history simulated. An illustration of this is provided by Fig. 7A where transient erosion rates of between ca. 10^4 mm/ka were inferred for a minimum duration of ca. ≤ 1 a, and extending up to ca. 10^3 mm/ka for durations up to ca. 50 a. Beyond ca. 50 a, a steady state of erosion was reached at a constant erosion rate of ca. 10^3 mm/ka, represented by the flattening of the profile with the highest likelihood. Alternatively, a profile indicative of a transient state of erosion where no steady state has been established is illustrated by Fig. 7D where transient erosion rates of between ca. 10^2 mm/ka were inferred for a minimum duration of ca. ≤ 1 a, and extending up to ca. 10^1 mm/ka for durations beyond ca. 200 a. This numerical approach (Lehmann et al. 2019a) allows erosion history to be considered as non-constant in time (i.e. transient), in addition to steady-state, and so it is more indicative of the stochastic erosional processes (driven by temperature, precipitation, snow cover, wind) in nature.

3. The Beinn Alligin rock avalanche

Today, average winter and summer temperatures in NW Scotland are 7°C and 18°C , respectively, while average annual precipitation (mostly rainfall) is high (ca. 2,300 mm/a) (Met Office, 2021). The Beinn Alligin rock avalanche ($57^\circ35'\text{N}$, $05^\circ34'\text{W}$) is a distinct, lobate deposit of large boulders that is 1.25 km long and covers an area of 0.38 km^2 (Fig. 1). It has

163 previously been ascribed various origins including a rockslide onto a former corrie glacier (e.g. Ballantyne, 1987; Gordon,
164 1993) and a former rock glacier (Sissons, 1975; 1976). However, on the basis of cosmogenic exposure dates that constrain its
165 deposition to the ~~Middle to~~ Late Holocene it is now widely accepted to have been deposited by a rock-slope failure that
166 experienced excess run-out (e.g. a rock avalanche). The source is a distinct, fault-bounded failure scar on the southern flank
167 of Sgurr Mor, the highest peak of Beinn Alligin (Ballantyne, 2003; Ballantyne and Stone, 2004). The rock avalanche is
168 comprised of large, poorly-sorted boulders and is calculated to comprise a total volume of $3.3 - 3.8 \times 10^6 \text{ m}^3$, equivalent to a
169 mass of 8.3 – 9.5 Mt (Ballantyne and Stone, 2004). The source lithology is Late Precambrian Torridonian sandstone strata.
170 The Torridonian sandstones are reddish or reddish brown terrestrial sedimentary rocks deposited under fluvial or shallow
171 lake conditions (Stewart, 1982). The sandstones maintained a common origin throughout deposition (Stewart, 1982) and are
172 thus largely consistent in mineralogy (dominated by quartz, and alkali and plagioclase feldspar) although there are some
173 local variations in grain size (Stewart and Donnellan, 1992).

174 The ^{10}Be concentrations of three boulders used for cosmogenic nuclide exposure dating were internally consistent
175 evidencing a single, catastrophic mass movement event which occurred $4.54 \pm 0.27 \text{ ka}$ (re-calculated from Ballantyne and
176 Stone, 2004). Consequently, the boulders were very unlikely to have previously been exposed to cosmic rays or sunlight
177 prior to transport and deposition. Moreover, the large size of the flat-topped boulders ($>2 \times 2 \times 2 \text{ m}$) and lack of finer
178 sediment matrix within the rock avalanche deposit, suggested that post-depositional movement or exhumation is unlikely.
179 The Torridonian sandstones are hard, cemented rocks (Stewart, 1984; Stewart and Donnellson, 1992) susceptible to granular
180 disintegration (e.g. Ballantyne and Whittington, 1987). Given its inland location, salt weathering is likely negligible.
181 Kirkbride and Bell (2010) estimated edge-rounding rates of $\sim 3.3 \text{ mm/ka}$ for a suite of Torridonian sandstone boulder
182 samples from a range of sites in NW Scotland under the warmer, wetter climates of the Holocene. A notably higher erosion
183 rate of 12 mm/ka was specifically determined for the Beinn Alligin rock avalanche. Kirkbride and Bell (2010) suggest that
184 this higher erosion rate, in comparison to the other sites, is likely due to inherited rock roundness caused by abrasion during
185 the high-magnitude depositional event. Additionally, minor differences in lithology cannot be ruled out (e.g. Twidale, 1982;
186 Ford and Williams, 1989). Consequently, we consider the range ~ 3.3 to 12 mm/ka as a reasonable estimation of the
187 Holocene erosion rate of the Torridonian sandstone boulders that comprise the Beinn Alligin rock avalanche.

188 **4. Methods**

189 A total of six rock samples were taken from the Torridonian sandstones in NW Scotland (Fig. 1). Three samples were taken
190 from three different road-cuttings of known age to calibrate the values of μ and $\overline{\sigma\phi_0}$: ROAD01 (0.01 a), ROAD02 (57 a; Fig.
191 S1a), ROAD03 (44 a; Fig. S1b). Three further samples were taken from flat-topped, angular boulders that were part of the
192 Beinn Alligin rock avalanche deposit: BALL01, BALL02 and BALL03 (Fig. 1D). Portions of the original boulder or
193 bedrock sample ~~Samples~~ were collected in the field in daylight and immediately placed into opaque, black sample bags. All
194 samples were taken from surfaces perpendicular to incoming sunlight to ensure that the daylight irradiation geometry was
195 similar between calibration and dating samples (cf. Gliganic et al. 2019).

196 4.1 Luminescence measurements

197 To calculate the environmental dose-rate throughout burial for each sample (Table 1), U, Th and K concentrations were
198 measured for ca. 80 g of crushed bulk sample using high-resolution gamma spectrometry. Internal dose-rates were calculated
199 assuming an internal K-content of 10 ± 2 % (Smedley et al. 2012) and internal U and Th concentrations of 0.3 ± 0.1 ppm and
200 1.7 ± 0.4 ppm (Smedley and Pearce, 2016), in addition to the measured average grain sizes for each sample. Cosmic
201 dose-rates were calculated after Prescott and Hutton (1994). For measuring the luminescence depth profiles, sample
202 preparation was performed under subdued-red lighting conditions to prevent contamination of the luminescence signal. Rock
203 cores ~7 mm in diameter and up to 20 mm long were drilled into the rock surface using an Axminster bench-top, pillar drill
204 equipped with a water-cooled, diamond-tipped drillbit (~9 mm diameter). Each core was sliced at a thickness of ~0.7 mm
205 using a Buehler IsoMet low-speed saw equipped with a water-cooled, 0.3 mm diameter diamond-tipped wafer blade. All
206 slices were then mounted in stainless steel cups for luminescence measurements.

207 Luminescence measurements were performed on a Risø TL/OSL reader (TL-DA-15) with a $^{90}\text{Sr}/^{90}\text{Y}$ beta irradiation
208 source. Heating was performed at $1^\circ\text{C}/\text{s}$ and the rock slices were held at the stimulation temperature (i.e. 50, 150 and 225°C)
209 for 60 s prior to IR stimulation to ensure all of the disc was at temperature before stimulating (cf. Jenkins et al. 2018). IRSL
210 signals were detected in blue wavelengths using a photo-multiplier tube fitted with Schott BG-39 (2 mm thickness) and
211 Corning 7-59 (2 mm thickness) filters. A MET-post-IR IRSL sequence (Table S1) was used to determine IRSL signals at
212 three different temperatures (50, 150 and 225°C) simultaneously/successively, hereafter termed the IR_{50} , pIRIR_{150} and
213 pIRIR_{225} signals. ~~OSL~~Luminescence depth profiles were determined for each core by measuring the natural signal (L_n)
214 normalised using the signal measured in response to a 53 Gy test-dose (T_n), hereafter termed the L_n/T_n signal. The IRSL
215 signal was determined by subtracting the background signal (final 20 s, 40 channels) from the initial signal (0 – 3.5 s, 7
216 channels). The large test-dose (53 Gy) was used to reduce the impact of thermal transfer/incomplete resetting of the IRSL
217 signal between measurements (after Liu et al. 2016).

218 D_e values were determined for the shallowest disc and the deepest disc from one core of each sample to quantify the
219 natural residual dose and saturation limit (L_0 , Eq. 1), respectively. Fading rates (g -values, Aitken 1985) were determined for
220 three discs of each sample and normalised to a t_c of two days (Huntley and Lamothe 2001). The weighted mean and standard
221 error of the g -values for all discs were 3.7 ± 0.4 %/dec. (IR_{50}), 1.0 ± 0.5 %/dec. (pIRIR_{150}) and 1.0 ± 0.5 %/dec. (pIRIR_{225}).
222 The large uncertainties on the individual g -values measured were derived from uncertainty in the fit of the data, which is
223 typical of fading measurements (e.g. Smedley et al. 2016). The fading rates were in line with previous measurements of
224 IRSL signals (e.g. Roberts 2012; Trauerstein et al. 2014; Kolb and Fuchs 2018). Lehmann et al. (2019a) performed
225 sensitivity tests of the shape of the luminescence depth profiles (IR_{50}) with a high and low g -value end-members and these
226 simulations demonstrated that athermal loss of signal has a minimal impact upon the IRSL depth profile shape; thus,
227 athermal loss (i.e. fading rates) was not considered in calculations.

228 Previous studies have shown that the IR₅₀ signal bleached faster than the pIRIR signals (Smedley et al., 2015). To
229 test the inherent bleaching rates of the feldspars in our samples, artificial bleaching experiments were performed on seven
230 discs from all six samples (n.b. these experiments do not test for variations in light attenuation with depth). All previously-
231 analysed discs were given a 105 Gy dose, then subjected to different exposure times in a solar simulator (0 m, 1 m, 10 m, 30
232 m, 1 h, 4 h and 8 h) and the normalised luminescence signals (IR₅₀, pIRIR₁₅₀ and pIRIR₂₂₅) were measured (Fig. S42). The
233 results show some variations after 1 m of solar simulator exposure. However, luminescence signals reduced to 2 – 6 %
234 (IR₅₀), 6 – 11 % (pIRIR₁₅₀) and 14 – 22 % (pIRIR₂₂₅) of the unexposed light levels after 1 h and 1 – 2 % (IR₅₀), 2 – 3 %
235 (pIRIR₁₅₀) and 4 – 7 % (pIRIR₂₂₅) after 8 h. This indicates that within our samples the minerals emitting the IRSL signals
236 (i.e. K-feldspar) have similar inherent bleaching rates when exposed to longer durations of time (i.e. > 8 h in the solar
237 simulator).

238 4.2 Rock composition

239 After luminescence measurements were performed, each rock slice (e.g. Fig. 2) was analysed to investigate potential changes
240 in rock composition with depth (inferred by opacity and grainsize). The average down-core grainsize of each sample was
241 measured under an optical microscope using Infinity Analyze. For each rock slice of an example core per sample, ten
242 randomly-selected grains were measured and the mean and standard deviation grainsize were calculated per core and plotted
243 against the core depths (Fig. 3B). Down-core red-green-blue (RGB) values were determined for each sample to investigate
244 whether there was any colour variation within the sample, and externally between samples; thus, providing a semi-
245 quantitative tool to detect variability in rock opacity (Meyer et al. 2018). Raster images of RGB were obtained for each rock
246 slice using an EPSON Expression 11000XL flatbed scanner at 1200 dpi resolution (e.g. Fig. S32). Mean and standard
247 deviations of the RGB values (e.g. Fig. 3A) for each rock slice were calculated using the *raster* package in R (version 2.9-
248 23; Hijmans, 2019).

249 5. Results

250 5.1 Luminescence depth profiles

251 The luminescence depth profiles (IR₅₀, pIRIR₁₅₀ and pIRIR₂₂₅) (Fig. 4) record bleaching fronts caused by sunlight exposure
252 for all of the known-age samples. The luminescence depth profile measured for core 3 of sample ROAD02 (Fig. 4
253 g-h,jG,H,J) was inconsistent with cores 1 and 2, giving high standard deviation values for the IR₅₀ (1.2), pIRIR₁₅₀ (1.1) and
254 pIRIR₂₂₅ (0.9) signals; thus, core 3 was removed from subsequent analysis (likely sample preparation issues related to
255 drilling preservation of the weathered surface). The luminescence depth profiles for the remaining replicate cores for all
256 three samples were broadly consistent within each rock sample with mean standard deviations ranging from 0.2 – 0.8.

257 The luminescence depth profiles (Fig. 4) for the IR₅₀ signal were consistent with the increasing sunlight exposure
258 ages for ROAD01 (0.01 a), ROAD03 (44 a) and ROAD02 (57 a), with bleaching fronts at 2.50.75 mm, 4.500 mm and 4.76-5
259 mm, respectively (Fig. S54a). This indicated that the depth of the IR₅₀ bleaching front was dominated by exposure duration
260 for the known-age samples as expected. Similarly, the pIRIR₁₅₀ and pIRIR₂₂₅ bleaching fronts were shallower in sample

ROAD01 (0.75±.5 mm) compared to ROAD02 and ROAD03 (2.5.00 – 33.500 mm), reflecting the younger exposure duration of ROAD01. However, the pIRIR₁₅₀ and pIRIR₂₂₅ bleaching fronts were at similar depths (23.75 and 3.00 mm and 2.005 and 2.50 mm respectively) for both ROAD02 (57 a) and ROAD03 (44 a). This suggests that either another factor is influencing light penetration with depth in these rocks (e.g. small differences in the orientation of the sampled rock faces; Fig. S1) or that the pIRIR signals cannot resolve between a 57 a and 44 a exposure history (difference of only 13 a). Note that the inferred models shown in Fig. 4 were fitted using the $\overline{\sigma\phi_0}$ and μ values included in each figure. See Section 5.2 for further explanation of the estimation of the model parameters.

The luminescence depth profiles measured for the unknown-age samples BALL02 and BALL03 using the IR₅₀, pIRIR₁₅₀ and pIRIR₂₂₅ signals (Fig. 5) recorded bleaching fronts caused by sunlight exposure. Conversely, the luminescence depth profile for sample BALL01 had saturated IRSL signals throughout the core and did not display any evidence of IRSL signal resetting with depth (Fig. 5aA-Ce). A luminescence depth profile measured for a core drilled into the bottom surface (Bottom C1; Fig. 5Aa-eC) confirmed that the bottom surface of BALL01 was also saturated. The lack of a bleaching front in sample BALL01 is difficult to explain as the sample was taken in daylight and had seemingly identical characteristics to samples BALL02 and BALL03 (i.e. no lichen-cover or coatings preventing light penetration in the rock). Although all the samples were similar in colour/opacity (Fig. 3Aa), the surface of sample BALL01 was coarser grained than BALL02 and BALL03 (Fig. 2; Fig. 3Bb). Studies have shown that coarser grain sizes are more susceptible to mechanical weathering via grain detachment induced by chemical weathering (Israelli and Emmanuel, 2018). Thus, although care was taken when sampling to mark the surface of the rock and to measure the length of the rock cores before and after slicing, it is possible that the luminescence depth profile (likely <10 mm based on BALL02 and BALL03) was lost during sampling and/or sample preparation due to the presence of a fragile weathering crust, potentially with a sub-surface zone of weakness (e.g. Robinson and Williams, 1987). Furthermore, field observations showed the presence of a rock pool on the surface of the boulder sampled for BALL01, which is not present on BALL02 and BALL03 (Fig. 1De); thus, there is also potential that the surface sampled for BALL01 had experienced enhanced chemical weathering via trickle paths draining the rock pool. These are commonly linked to a greater density of micro-cracks in the uppermost mm's-millimetres of the rock (Swantesson, 1989, 1992). Consequently, we did not derive exposure ages or erosion rates from BALL01. Where rock pools are likely on boulders, the highest rock surface should be sampled for luminescence techniques to avoid the potential for pooling or trickle paths.

5.2 Estimation of model parameters

To determine an apparent exposure age or erosion rate from the measured luminescence depth profiles, the variables that control the evolution of a luminescence depth profile in a rock surface must be parameterised; specifically, the dose-rate (\dot{D}) (see Section 4.1), saturation level (D_0), $\overline{\sigma\phi_0}$ and μ . D_0 was determined experimentally from saturated dose-response curves measured for the deepest rock slices of each sample. $\overline{\sigma\phi_0}$ and μ were calibrated using Eq. (1) and the known-age samples (ROAD01, ROAD02 and ROAD03) of similar, suitable rock composition as determined by the down-core profiles of RGB

294 and grainsize (Section 4.2). Note that (\dot{D}) is not considered in Eq. (1) but is used to determine an apparent exposure age or
295 erosion rate and so needs to be measured for each sample (see Section 2). Down-core RGB values for all samples were
296 internally consistent (Fig. 3aA) as indicated by the relative standard deviation (RSD) range between 8 and 12 %. The down-
297 core RGB values were also externally consistent between all samples (Fig. 3Aa), with the exception of the slightly darker-
298 coloured sample ROAD01. However, measurements of grainsize (Fig. 3bB) showed that the known-age sample ROAD02
299 ($90 \pm 23 \mu\text{m}$) had a similar grainsize to the unknown-age samples BALL02 ($73 \pm 18 \mu\text{m}$) and BALL03 ($98 \pm 19 \mu\text{m}$),
300 whereas ROAD01 ($42 \pm 9 \mu\text{m}$) and ROAD03 ($168 \pm 56 \mu\text{m}$) were finer and coarser grained, respectively. Given the
301 similarity in colour and grain-size, it was considered most appropriate to calibrate $\overline{\sigma\varphi_0}$ and μ for the unknown age samples
302 (BALL02 and BALL03) using known-age sample ROAD02.

303 The values of $\overline{\sigma\varphi_0}$ and μ were determined by fitting Eqn. (1) using the approach of Lehmann et al. (2019a). The
304 inferred model (Eq. 1) had a good fit to the measured data for all samples and signals (Fig. 4) and μ and $\overline{\sigma\varphi_0}$ were calculated
305 (Table 2; Fig. 6). For ROAD01, the parameters determined using the IR₅₀ ($\mu = 3.2 \text{ mm}^{-1}$, $\overline{\sigma\varphi_0} = 2.80e^{-4} \text{ s}^{-1}$), pIRIR₁₅₀ ($\mu =$
306 3.1 mm^{-1} , $\overline{\sigma\varphi_0} = 3.27e^{-5} \text{ s}^{-1}$) and pIRIR₂₂₅ ($\mu = 3.0 \text{ mm}^{-1}$, $\overline{\sigma\varphi_0} = 2.88e^{-5} \text{ s}^{-1}$) signals were broadly consistent. For ROAD02,
307 the parameters differed between the IR₅₀ ($\mu = 2.1 \text{ mm}^{-1}$, $\overline{\sigma\varphi_0} = 6.67e^{-6} \text{ s}^{-1}$), pIRIR₁₅₀ ($\mu = 1.5 \text{ mm}^{-1}$, $\overline{\sigma\varphi_0} = 1.73e^{-8} \text{ s}^{-1}$) and
308 pIRIR₂₂₅ ($\mu = 2.8 \text{ mm}^{-1}$, $\overline{\sigma\varphi_0} = 9.01e^{-8} \text{ s}^{-1}$) signals, but the values for each signal were broadly similar to the equivalent
309 values determined for ROAD03 using the IR₅₀ ($\mu = 2.7 \text{ mm}^{-1}$, $\overline{\sigma\varphi_0} = 1.56e^{-5} \text{ s}^{-1}$), pIRIR₁₅₀ ($\mu = 1.5 \text{ mm}^{-1}$, $\overline{\sigma\varphi_0} = 3.80e^{-8} \text{ s}^{-1}$)
310 and pIRIR₂₂₅ ($\mu = 1.4 \text{ mm}^{-1}$, $\overline{\sigma\varphi_0} = 1.70e^{-8} \text{ s}^{-1}$) signals. Given the similarity of $\overline{\sigma\varphi_0}$ and μ determined using all three IRSL
311 signals for ROAD02 and ROAD03 and the difference in grain sizes (Fig. 3B), it suggests that grain size has a minimal impact
312 upon the attenuation of light into a rock surface in comparison to other factors (e.g. mineralogy, surficial coatings). The μ
313 values for samples ROAD01, ROAD02 and ROAD03 determined using the IR₅₀ signal in this study were comparable to μ
314 values in existing literature for sandstones using K-feldspar e.g. $\mu = 1.01 \text{ mm}^{-1}$ where $\overline{\sigma\varphi_0} = 6.80e^{-9} \text{ s}^{-1}$ (Sohbati et al. 2012)
315 and 3.06 mm^{-1} (Ou et al. 2018). For sample ROAD01, μ and $\overline{\sigma\varphi_0}$ were similar for all three IRSL signals with large
316 uncertainties (Fig. 6Aa-eC) which is likely related to the shorter exposure age of this sample (0.01 a). The finer grain size
317 and darker rock opacity of sample ROAD01 in comparison to ROAD02 and ROAD03 likely explained the larger values of μ
318 (i.e. greater light attenuation with depth into the rock surface).

319 5.3 Apparent exposure ages and erosion rates

320 Luminescence exposure ages were determined from the luminescence depth profiles using μ and $\overline{\sigma\varphi_0}$ derived from sample
321 ROAD02 for each of the IRSL signals (Table 3). For BALL03, the IR₅₀ ($3787 \pm 10345 \text{ a}^+$), pIRIR₁₅₀ ($2964 \pm 6154 \text{ a}^+$) and
322 pIRIR₂₂₅ ($37062 \pm 469 \text{ a}^+$) signals all gave luminescence exposure ages in agreement within uncertainties. For BALL02, the
323 three signals were inconsistent with one another. The pIRIR₂₂₅ signal ($27963 \pm 4830 \text{ a}^+$) was consistent with BALL03, but
324 the IR₅₀ ($89 \pm 23 \text{ a}^+$) and pIRIR₁₅₀ ($7066 \pm 916 \text{ a}^+$) signals for BALL02 were younger than BALL03. All apparent exposure
325 ages based on the different luminescence signals were at least one order of magnitude younger than the apparent exposure
326 age based cosmogenic nuclide dating ($4.54 \pm 0.27 \text{ ka}$; Ballantyne and Stone, 2004). This was likely because erosion over

327 time in this wet, temperate climate has removed material from the surface of the rock and created shallower luminescence
328 depth profiles in comparison to a non-eroding profile; thus, the luminescence depth profile is dependent upon both exposure
329 age and the erosion rate (Sohbati et al. 2018; Lehmann et al. 2019a).

330 To test whether erosion rates could be determined for the Beinn Alligin boulders from the luminescence depth
331 profiles, we performed erosion rate modelling following the inversion approach of Lehmann et al. (2019) and constrained by
332 the re-calculated cosmogenic nuclide age (Ballantyne and Stone, 2004). This approach defines an erosion history that
333 follows a step function with an initial period of zero erosion, followed by an immediate increase to a constant erosion rate at
334 a defined time. It attempts to recover parameter combinations (erosion rate and timing of erosion initiation) that are both
335 consistent with the cosmogenic nuclide concentration and produce modelled luminescence profiles that match observations.
336 For ~~sample~~ BALL02, both the IR₅₀ and pIRIR₁₅₀ signals suggested that the system had approached a steady-state with erosion
337 rates of 66 mm/ka (IR₅₀) and 9 mm/ka (pIRIR₁₅₀) applied over time periods >73 a and 593 a, respectively. However, the
338 pIRIR₂₂₅ signal suggested a transient erosion state, where the luminescence signal could be derived from numerous pairs of
339 erosion rates and initiation times from a maximum erosion rate of 310 mm/ka over a minimum time interval of 4 a to a
340 minimum erosion rate of 12 mm/ka over a minimum time interval of 90 a. All three IRSL signals from sample BALL03
341 consistently suggested a system undergoing a transient response to erosion, which was consistent with the pIRIR₂₂₅ signal of
342 BALL02 (Fig. 7, Table 3). The IR₅₀ signal for BALL03 derived a maximum erosion rate of 460 mm/ka over a minimum
343 time interval of 3 a and a minimum erosion rate of 6 mm/ka over a minimum time interval of 231 a. The pIRIR₁₅₀ signal for
344 BALL03 derived a maximum erosion rate of 100 mm/ka over minimum time interval of 19 a and a minimum erosion rate of
345 14 mm/ka over a minimum time interval of 137 a. The pIRIR₂₂₅ signal for BALL03 derived a maximum erosion rate of 180
346 mm/ka over a minimum time interval of 4 a and a minimum erosion rate of 11 mm/ka over a minimum time interval of 73 a.

347 At face value, the fit of the inferred erosion model to the experimental data for BALL02 using the IR₅₀ (Fig. 5D)
348 and pIRIR₁₅₀ (Fig. 5E) signals is better than the equivalent fits for BALL02 using the pIRIR₂₂₅ signal (Fig. 5F) and BALL03
349 using the IR₅₀ (Fig. 5G), pIRIR₁₅₀ (Fig. 5H) and pIRIR₂₂₅ (Fig. 5I) signals. In the latter cases, the inferred erosion model is
350 shallower than the experimental data. This could suggest that the $\overline{\sigma\phi_0}$ and μ values were inaccurate, i.e. the attenuation of
351 light with depth into the rock surface is lower in BALL02 (pIRIR₂₂₅ signal) and BALL03 (IR₅₀, pIRIR₁₅₀ and pIRIR₂₂₅
352 signals) than estimated by ROAD02. A possible explanation for this is that the surface of the roadcut sampled by ROAD02
353 (Fig. S1a) was orientated slightly differently to the Beinn Alligin rock avalanche boulders sampled by BALL02 and
354 BALL03 (Fig. 1D), relative to the incoming sunlight (e.g. Gliganic et al. 2019). However, if the orientation of the known-age
355 roadcut samples was even slightly inconsistent with the unknown samples, we would expect these inconsistencies to
356 manifest similarly in all three MET signals for BALL02 and BALL03, which was not observed here. A factor that is
357 common to all the less wellpoorly fitting profiles that are less well fit by the inferred erosion model is that they
358 determineddefine transient erosion ratesstates. This suggests that these surfaces experienced complex erosional histories over
359 time whereby the erosion rate was time-varying. Consequently, it is possible that surficial weathering products may have

360 changed in thickness and composition over time, which in turn could slightly vary the attenuation of light (Meyer et al. 2018;
361 Luo et al. 2018), meaning that the calibration of $\overline{\sigma\varphi_0}$ and μ from ROAD02 here introduced uncertainty into the inferred
362 erosion model as it was not time-varying. It is also possible that sample-specific measurements of $\overline{\sigma\varphi_0}$ and μ (e.g. Ou et al.
363 2018), rather than calibration from known-age samples, could reduce the uncertainty introduced by time-varying light
364 attenuation. However, further investigation is required into the physical mechanisms of time-varying light attenuation in the
365 context of surficial weathering and subsequent erosion, and the impacts upon inferred transient erosion rates.

367 **6. Discussion**

368 **6.1 Luminescence depth profiles ~~at for the~~ Beinn Alligin rock avalanche**

369 Despite the similarity in rock opacity, grain-size, aspect and exposure history, the luminescence depth profiles for samples
370 BALL02 and BALL03 from the Beinn Alligin rock avalanche were inconsistent (Fig. 5). We consider it unlikely that this
371 lack of consistency was caused by local variations in erosion rates (e.g. due to microclimate, aspect etc; Hall et al. 2005,
372 2008) as there were discrepancies between all three IRSL signals of BALL02. We would expect local erosion rate variations
373 between samples to be consistently recorded across each of the IRSL signals, assuming the model parameterisation (μ and
374 $\overline{\sigma\varphi_0}$) were accurate. Specifically, and with all other things being equal, a locally-variable erosion rate would translate the
375 bleaching front(s) closer to the rock surface by a proportionally consistent amount for each signal of a given sample.

376 Analysis of the rock opacity with depth (Section 4.2; Meyer et al. 2018) showed that sample BALL02 was more
377 positively skewed towards darker colours than ROAD02 and BALL03 (Fig. S32, S34), with higher surficial values caused
378 by Fe-staining. Fe-staining can occur on rock surfaces with seasonal rock pools and trickle paths (Swantesson, 1989, 1992).
379 The presence of a thin Fe-coating (<1 mm) on the rock surface would have changed the intensity and wavelength of the net
380 daylight flux received by individual grains (e.g. Singhvi et al., 1986; Parish, 1994) and likely increased light attenuation with
381 depth (e.g. Meyer et al. 2018; Luo et al. 2018). Consequently, the parameterisation of μ and $\overline{\sigma\varphi_0}$ derived from sample
382 ROAD02 would be inaccurate for BALL02. Interestingly, the similarity between BALL02 and BALL03 for the pIRIR₂₂₅
383 signal suggests that the presence of an Fe-coating altered may have preferentially attenuated the wavelengths that influence
384 the attenuation of the IR₅₀ and pIRIR₁₅₀ signals to a lesser extent than, and not the pIRIR₂₂₅ signal, but the reasons for this
385 requires further investigation. The application of the MET-pIRIR rather than just the stand-alone IR₅₀ signal protocol
386 provided a major advantage as it identified samples where the parameterisation of μ and $\overline{\sigma\varphi_0}$ from known-age samples was
387 complicated by factors such as surficial weathering coatings. Beyond this, it is possible that the MET-pIRIR protocol may be
388 useful in identifying complex burial or exposure histories of rocks, similar to those that have been reported in previous
389 studies but solely using the IR₅₀ signal (e.g. Freiesleben et al. 2015; Brill et al. 2021). There is also potential to explore
390 whether the different temperature IRSL signals of the MET protocol record different states of erosion (i.e. steady or transient
391 states) within the same rock surface, whereby the post-IR IRSL signals that are attenuated greater would be more susceptible

392 to transient states of erosion in comparison to the lower temperature signals, which measure luminescence depth profiles to
393 greater depths within the rock surface.

394 The boulders from the Beinn Alligin rock avalanche have been subject to a temperate climate for the last ~4 ka. The
395 luminescence depth profiles from the boulders demonstrated that on these timeframes and under these climatic conditions the
396 technique was an erosion-meter, rather than a chronometer, as expected (Sohbati et al. 2018; Lehmann et al. 2019a).
397 Lehmann et al. (2018~~9~~a) noted that two of their samples, uncorrected for erosion, gave apparent luminescence exposure ages
398 of ca. 640 a and <1 a compared to apparent TCN-cosmogenic nuclide ages of ca. 16.5 ka and 6.5 ka, respectively. It has thus
399 been inferred that erosion rates >1 mm/ka can make interpretation of luminescence depth profiles in terms of an exposure age
400 difficult without accurately constraining the erosion rate (Sohbati et al., 2018; Lehmann et al., 2018). This is consistent with
401 the underestimation of luminescence exposure ages measured here for the Beinn Alligin rock avalanche (Table 3), which
402 have been independently-dated to 4.54 ± 0.27 ka using cosmogenic nuclides (Ballantyne and Stone, 2004). Consequently,
403 luminescence depth profiles for the Beinn Alligin rock avalanche can only be inferred in terms of erosion rates.

404 **6.2 Luminescence as an erosion-meter**

405 The numerical approach of Lehmann et al. (2019a) exploits the different sensitivities of the luminescence (short-term) and
406 cosmogenic nuclide (longer-term) techniques to erosion to infer erosion histories (steady state and transient over time) for
407 rock surfaces. Their modelling shows that the higher erosion rates (>100 mm/ka) can only be sustained over shorter time
408 durations (up to decadal) while at the same time being consistent with cosmogenic nuclide measurements. For BALL03,
409 transient erosion rates were derived using the IR₅₀ (6 - 460 mm/ka), pIRIR₁₅₀ (14 - 100 mm/ka) and pIRIR₂₂₅ (11 - 180
410 mm/ka) signals. These modelled transient erosion rates were broadly comparable to erosion rates inferred from luminescence
411 depth profiles over comparable timeframes in previous studies: (i) rates between $<0.038 \pm 0.002$ and 1.72 ± 0.04 mm/ka for
412 glacial boulders and landslides (granite gneiss, granodiorite and quartzite) in the Eastern Pamirs, China (Sohbati et al. 2018);
413 and (ii) between 3.5 ± 1.2 mm/ka and $4,300 \pm 600$ mm/ka for glacially-modified, granitic bedrock in the French Alps
414 (Lehmann et al., 2019b). This latter study modelled higher erosion rates (>100 mm/ka) over timescales from 10¹ to 10³ a and
415 lower erosion rates (<100 mm/ka) over longer time scales of 10³ to 10⁴ a. However, this comparison between modelled
416 erosion rates does not account for the primary role that lithology has on weathering (e.g. Twidale, 1982; Ford and Williams,
417 1989). The sampled boulders in our study were composed of Torridonian sandstone, which has been reported to undergo
418 granular disintegration (e.g. Ballantyne and Whittington, 1987), particularly around edges, and thus may have experienced
419 higher erosion rates than the crystalline rocks (e.g. gneiss, granite) used in the studies of Sohbati et al. (2018) and Lehmann
420 et al., 2019b.

421 A major advantage of applying this new erosion-meter technique to boulders of the Beinn Alligin rock avalanche
422 was the existing constraints on Holocene erosion rates (~3.3 to 12 mm/ka) for Torridonian sandstones in NW Scotland
423 inferred from boulder edge roundness measurements (Kirkbride and Bell, 2009). The long-term erosion rates inferred from
424 luminescence depth profiles were consistent with the estimates provided by measuring the boulder-edge roundness, when

425 considering the differing approaches and assumptions of each method. Firstly, the sampling approach for the luminescence
426 depth profiles targeted the flat-top surface of the boulders where granular disintegration would have been reduced relative to
427 the boulder edges and corners. Thus, the boulder-edge roundness based erosion rates provided an upper constraint on the
428 long-term erosion rate experienced by the boulders. Finally, the boulder-edge roundness measurements assumed steady-state
429 erosion and could not identify the potential for a transient state of erosion, whereas the approach of Lehmann et al. (2019a,b)
430 inferred some transient state of erosion (Table 3). Consequently, it is notable that the lower range of the transient erosion
431 rates derived here using the IR₅₀ (6 - 460 mm/ka), pIRIR₁₅₀ (14 - 100 mm/ka) and pIRIR₂₂₅ (11 - 180 mm/ka) signals were
432 broadly consistent with the steady-state erosion rate derived from boulder edge roundness measurements for the Torridonian
433 sandstones (in the range of ca. 3.3 to 12.0 mm/ka). Lehmann et al. (2019b) noted that their modelled steady-state erosion
434 rates were one to two orders of magnitude higher than suggested by a global compilation of bedrock surface erosion rates
435 based on ¹⁰Be (Portenga and Bierman, 2011), and measurements of upstanding, resistant lithic components (ca. 0.2 – 5.0
436 mm/ka) in crystalline rock surfaces in Arctic Norway (André, 2002). The authors inferred that shorter-term erosion rates
437 derived from luminescence measurements were higher than the longer-term averages due to the stochastic nature of
438 weathering impacting upon shorter-term erosion rates, this is also suggested by the data presented here. These stochastic
439 processes (i.e. varying over time) will be controlled by the in-situ weathering rates, which provided the material for erosion.
440 For bare rock surfaces in wet, temperate climates, weathering rates are primarily driven by rock-type and moisture
441 availability (i.e. precipitation) (Hall et al. 2012; Swantesson, 1992). The Torridonian sandstones are hard, cemented rocks
442 (Stewart, 1984; Stewart and Donnellson, 1992) susceptible to granular disintegration (e.g. Ballantyne and Whittington,
443 1987), which may have been stochastic in nature due to changing moisture availability for chemical weathering over time
444 (Hall et al. 2012; Swantesson, 1992). Although ~~the~~ Torridonian sandstones ~~is~~ are unlikely to be prone to frost shattering due
445 to ~~its~~ their low permeability and porosity (Lautridou, 1985; Hudec 1973 in Hall et al. 2012), cracks, faults and joints in the
446 rock may have facilitated stochastic physical weathering (Swantesson 1992; Whalley et al. 1982), but little field evidence of
447 this was preserved.

448 The modelled erosion histories that we have calculated here using the luminescence erosion-meter for samples
449 BALL02 and BALL03 would have had a minimal effect upon the cosmogenic nuclide exposure age (4.54 ± 0.27 ka;
450 Ballantyne and Stone, 2004). Only the steady-state erosion rate of 66 mm/ka inferred for BALL02 using the IR₅₀ signal,
451 when applied for durations exceeding 1 ka, would ~~have~~ increase ~~d~~ the exposure age to any great degree. For example, when
452 the steady-state erosion rate of 66 mm/ka was applied for 0.1 ka, the corrected cosmogenic nuclide exposure age would have
453 been 4.58 ka and, when the same erosion rate was applied for 1 ka it would have been 4.99 ka; these corrected ages were
454 consistent within $\pm 2 \sigma$ uncertainties of the uncorrected age of 4.54 ± 0.27 ka (reported at 1σ : Ballantyne and Stone, 2004).
455 The higher, transient erosion rates inferred for BALL03 were all applied for such a short period of time (e.g. Table 3) that
456 they had a minimal effect on the cosmogenic nuclide exposure age.

457 Based on the long-term erosion rates derived here, the boulder sampled for BALL02 would have lost a total of 300
458 mm (IR₅₀), 41 mm (pIRIR₁₅₀) and 54 mm (pIRIR₂₂₅) from the surface over 4.54 ka, while the long-term erosion rates
459 determined for BALL03 suggested that the boulder surface would have lost 27 mm (IR₅₀), 64 mm (pIRIR₁₅₀) and 50 mm
460 (pIRIR₂₂₅). All of these values (except for the IR₅₀ signal of BALL02) were broadly consistent with field observations of
461 quartz protrusions on the surface of boulders >2 x 2 x 2 m that were densely distributed within the rock avalanche feature
462 (Fig. 1). Alternatively, the maximum (shorter-term) erosion rate end members of the transient erosion histories would have
463 removed 1407 mm (BALL02, pIRIR₂₂₅), 2088 mm (BALL03, IR₅₀), 454 mm (BALL03, pIRIR₁₅₀) and 817 mm (BALL03,
464 pIRIR₂₂₅) from the boulder surface over the 4.54 ka. These large values were inconsistent with field evidence and so
465 indicative of the transient state of erosion where high erosion rates were only sustained over short periods of time.
466

467 **6.3 Late Holocene erosion history**

468 The transient state of erosion inferred by the rock luminescence measurements reflected the stochastic nature of erosion over
469 the last 4 ka, where a lower time-averaged erosion rate was interrupted by discrete intervals of higher time-averaged erosion
470 rates. Rock weathering would have been dependent upon a variety of factors, primarily rock type and climate (Merrill 1906).
471 The main constituents of the Torridonian sandstones are quartz, alkali and plagioclase feldspar (mostly albite), with
472 precipitated quartz cementing the rock being resistant to chemical weathering (Stewart and Donnellan, 1992). However, the
473 red colouring of the sandstones represents the presence of Fe within the rock (Stewart and Donnellan, 1992), which is prone
474 to chemical weathering via oxidation and reduction. Field evidence of quartz grain protrusions on the rock surfaces (Fig. 1)
475 indicated that granular disintegration, rather than flaking or shattering, was the likely weathering process that produced
476 material for erosion on these hard boulders (e.g. Swantesson, 1992). This is also supported by a lack of shattered material
477 surrounding the large sampled boulders (and in fact on much of the Beinn Alligin rock avalanche deposit), despite the
478 presence of dense, low-level vegetation surrounding the boulders (e.g. Fig. S6). Granular disintegration has been reported as
479 responsible for much of the general microweathering in the temperate climate of Southern and Central Sweden during the
480 Holocene (e.g. Swantesson, 1992).

481 Given the coupling between precipitation, ~~mean annual~~ temperature and erosion (e.g. Reiners et al., 2003; Portenga
482 and Bierman, 2011), the stochastic processes producing transient erosion can relate to varying environmental conditions
483 (Hall et al. 2012; Swantesson, 1992; Whalley et al. 1982). In an environment where moisture is abundant due to high
484 precipitation rates (e.g. for NW Scotland, annual precipitation rates between 1981 and 2010 were ca. 2,300 mm/a; Met
485 Office, 2021), chemical weathering dominates: this is, as also reported for Holocene weathering processes in Sweden
486 (Swantesson, 1989, 1992). Moisture availability, rather than temperature, is the limiting factor as studies have reported the
487 presence of chemical weathering in natural settings subject to sub-zero temperatures (e.g. northern Canada, Hall, 2007;
488 Antarctica, Balke et al. 1991). Proxy evidence from across the British Isles records variability in temperature and
489 precipitation rates over the last 4.5 ka, where key increases in precipitation occurred at 2,750, 1,650 and 550 cal. years BP

490 correlated to Bond cycles (Charman, 2010). Thus, the transient erosion rates measured from boulders of the Beinn Alligin
491 avalanche were potentially a representation of the fluctuations in moisture availability experienced over the last 4.5 ka. Such
492 processes can only be inferred from luminescence depth profiles as they are sensitive to changing erosion on shorter
493 timeframes than all other techniques.

494 **7. Conclusion**

495 This study applies ~~the~~ new rock luminescence techniques to a well-constrained test scenario provided by flat-topped boulders
496 from the Beinn Alligin rock avalanche in NW Scotland (a wet, temperate climate), which are lithologically consistent
497 (Torridonian sandstones), have known-age road-cuts for parameterisation of μ and $\overline{\sigma\phi_0}$, have known cosmogenic nuclide
498 exposure ages (4.54 ± 0.27 ka) and independently-derived Holocene erosion rates (ca. 3.3 to 12.0 mm/ka). Applying the rock
499 luminescence techniques for exposure dating underestimated the cosmogenic nuclide ages for the Beinn Alligin rock
500 avalanche expected due to high erosion rates (as supported by field evidence of quartz grain protrusions on the rock
501 surfaces). Alternatively, the erosion rates determined were consistent with expected rates that were independently measured
502 in the field from boulder-edge roundness when considering the relative timescales of the time-averaged erosion rates. The
503 findings show that the luminescence erosion-meter has the resolution and sensitivity required to detect transient erosion of
504 boulders over the last 4.5 ka. The transient erosion rates -reflecting the stochastic nature of erosional processes in the wet,
505 temperate region of NW Scotland, likely in response to the known fluctuations in moisture availability (and to a lesser extent
506 temperature), which control the extent of chemical weathering. This study demonstrates that the luminescence erosion-meter
507 has huge potential for inferring erosion rates on sub-millennial scales for both steady-state and transient states of erosion (i.e.
508 stochastic processes), which is currently impossible with other techniques. Larger sample populations and careful sampling
509 of rock surfaces (avoiding the potential for rock pools and trickle paths) will likely be key for accurate measurements of
510 landscape-scale erosion, and the use of a MET-pIRIR protocol (50, 150 and 225 °C) is advantageous as it can identify
511 samples suffering from the complexities introduced by within-sample variability (e.g. surficial coatings).

512

513 **Author contributions**

514 RS, DS and RSJ were involved in project conception. RS, DS, RSJ and SB performed the field sampling. RS, DS, JB and GJ
515 performed the measurements, analysis and interpretations. All authors contributed to the writing of the manuscript, including
516 the preparation of figures.

517

518 **Acknowledgments**

519 Field and laboratory work was funded by Durham University Department of Geography Research Development Fund to DS.
520 The rock luminescence equipment in the Liverpool Luminescence Laboratory was funded by a Royal Society Research
521 Grant (RG170194) to RKS. DS is supported by a NERC Independent Research Fellowship NE/T011963/1. We thank

522 [Benjamin Lehmann, an anonymous reviewer and the Associate Editor Jim Feathers for their constructive comments which](#)
523 [improved this manuscript.](#)

525 References

- 526 Aitken, M.J. 1985. Thermoluminescence dating: Past progress and future trends. *Nuclear Tracks and Radiation*
527 *Measurements*, 10, 3-6.
- 528 André, M.-F. 2002. Rates of postglacial rock weathering of granite roches moutonnées in northern Scandinavia (Abisko-
529 Riksgränsen area, 68°N). *Geografiska Annaler* 64A, 139–150.
- 530 Balke, J., Haendel, D., Krüger, W. 1991. Contribution to the weathering-controlled removal of chemical elements from the
531 active debris layer of the Schirmacher Oasis, East Antarctica. *Zeitschrift für Geologische Wissenschaften*, 19, 153–158.
- 532 Ballantyne, C.K. 1987. The Beinn Alligin 'rock glacier'. In Ballantyne, C.K. and Sutherland, D.G., editors, *Wester Ross: field*
533 *guide*, Cambridge: Quaternary Research Association, 134-37.
- 534 Ballantyne, C.K. 2002. Paraglacial geomorphology. *Quaternary Science Reviews*, 21, 1935-2017.
- 535 Ballantyne, C.K. 2003. A Scottish sturzstrom: The Beinn Alligin rock avalanche, Wester Ross. *Scottish Geographical*
536 *Journal*, 119, 159-167.
- 537 Ballantyne, C.K., Whittington, G. 1987. Niveo-aeolian sand deposits on An Teallach, Wester Ross, Scotland. *Earth and*
538 *Environmental Science Transactions of The Royal Society of Edinburgh*, 78, 51 – 63.
- 539 Ballantyne, C.K., Stone, J.O. 2004. The Beinn Alligin rock avalanche, NW Scotland: cosmogenic ¹⁰Be dating, interpretation
540 and significance. *The Holocene*, 14, 448-453.
- 541 Bennett, M.R., Boulton, G.S. 1993. Deglaciation of the Younger Dryas or Loch Lomond Stadial ice-field in the northern
542 Highlands, Scotland. *Journal Quaternary Science*, 8, 133–145.
- 543 Bowen, D.Q. 1992. The Pleistocene of North West Europe. *Science Progress*, 76, 209-223.
- 544 [Brill, D., May, S.M., Mhammedi, N., King, G., Lehmann, B., Burow, C., Wolf, D., Zander, A., Brückner, H. 2021. Evaluating](#)
545 [optically stimulated luminescence rock surface exposure dating as a novel approach for reconstructing coastal boulder](#)
546 [movement on decadal to centennial timescales. *Earth Surface Dynamics*, 9, 205-234.](#)
- 547 [Brown, N.D. 2020. Which geomorphic processes can be informed by luminescence measurements. *Geomorphology*, 367,](#)
548 [107296.](#)
- 549 [Brown, N.D., Moon, S. 2019. Revisiting erosion rate estimates from luminescence profiles in exposed bedrock surfaces](#)
550 [using stochastic erosion simulations. *Earth and Planetary Science Letters*, 528, 115842.](#)
- 551 Chapot, M.S., Sohbaty, R., Murray, A.S., Pederson, J.L., Rittenour, T.M. 2012. Constraining the age of rock art by dating a
552 rockfall event using sediment and rock-surface luminescence dating techniques. *Quaternary Geochronology*, 13, 18-25.
- 553 Charman, D. 2010. Centennial climate variability in the British Isles during the mid-late Holocene. *Quaternary Science*
554 *Reviews*, 29, 1539-1554.
- 555 Esri. "World Imagery" [basemap]. Scale Not Given. "World Imagery". December 12, 2009.
556 https://services.arcgisonline.com/ArcGIS/rest/services/World_Imagery/MapServer. (Feb, 11, 2021).
- 557 Esri. "Topographic" [basemap]. Scale Not Given. "World Topographic Map". June 14, 2013.
558 <http://www.arcgis.com/home/item.html?id=30e5fe3149c34df1ba922e6f5bbf808f>. (Feb, 11, 2021).
- 559 Ford, D., Williams, P. 1989. *Karst Geomorphology and Hydrology*. Unwin Hyman, London. 601 pp.
- 560 [Freiesleben, T., Sohbaty, R., Murray, A., Jain, M., al Khasawneh, S., Hvidt, S., Jakobsen, B. 2015. Mathematical model](#)
561 [quantifies multiple daylight exposure and burial events for rock surfaces using luminescence dating. *Radiation*](#)
562 [Measurements, 81, 16-22.](#)
- 563 Gliganic, L.A., Meyer, M.C., Sohbaty, R., Jain, M., Barrett, S. 2019. OSL surface exposure dating of a lithic quarry in Tibet:
564 Laboratory validation and application. *Quaternary Geochronology*, 49, 199-204.
- 565 Gollledge, N.R., Hubbard, A., Sugden, D.E. 2008. High-resolution numerical simulation of Younger Dryas glaciation in
566 Scotland. *Quaternary Science Reviews*, 27, 888-904.
- 567 Gordon, J.E. 1993. Beinn Alligin. In Gordon, J.E. and Sutherland, D.G., editors *Quaternary of Scotland*, London: Chapman
568 and Hall, 118-22.

- 569 Habermann, J., Schilles, T., Kalchgruber, R., Wagner, G.A., 2000. Steps towards surface dating using luminescence.
570 Radiation Measurements 32, 847-851.
- 571 Hall, K. 2007. Evidence for freeze-thaw events and their implications for rock weathering in northern Canada, II: the
572 temperature at which water freezes in rock. *Earth Surface Processes and Landforms*, 32, 249–259.
- 573 Hall, K., Arocena, J.M., Boelhouwers, J., Zhu, L. 2005. The influence of aspect on the biological weathering of granites:
574 observations from the Kunlun Mountains, China. *Geomorphology*, 67, 171–188.
- 575 Hall, K., Guglielmin, M., Strini, A. 2008. Weathering of granite in Antarctica II: thermal data at the grain scale. *Earth
576 Surface Processes and Landforms*, 33, 475–493.
- 577 Hall, K., Thorn, C., Sumner, P. 2012. On the persistence of ‘weathering’. *Geomorphology*, 149-150, 1-10.
- 578 Hanna, F.K. 1966. A technique for measuring the rate of erosion of cave passages. *Proceedings University of Bristol
579 Speleology Society*, 11, 83–86.
- 580 Herman, F., Rhodes, E.J., Braun, J., Heiniger, L. 2010. Uniform erosion rates and relief amplitude during glacial cycles in
581 the Southern Alps of New Zealand, as revealed from OSL-thermochronology. *Earth and Planetary Science Letters*, 297,
582 183-189.
- 583 High, C.J., Hanna, F.K. 1970. A method for the direct measurement of erosion on rock surfaces. *British Geomorphological
584 Research Group Technical Bulletin*, 5, 1–25.
- 585 Hijmans, R.J. (2019). raster: Geographic Data Analysis and Modeling. R package version 2.9-23. [https://CRAN.R-](https://CRAN.R-project.org/package=raster)
586 [project.org/package=raster](https://CRAN.R-project.org/package=raster)
- 587 Huntley, D.J., Lamothe, M. 2001. Ubiquity of anomalous fading in K-feldspars and the measurement and correction for it in
588 optical dating, 38, 1093-1106.
- 589 Israelli, Y., Emmanuel, S. 2018. Impact of grain size and rock composition on simulated rock weathering. *Earth Surface
590 Dynamics*, 6, 319-327.
- 591 Jenkins, G. T. H., Duller, G. A. T., Roberts, H. M., Chiverrell, R. C., Glasser, N. F. 2018. A new approach for luminescence
592 dating glaciofluvial deposits – High precision optical dating of cobbles. *Quaternary Science Reviews*, 192, 263 – 273.
- 593 Kirkbride, M.P., Bell, C.M. 2010. Edge-roundness of boulders of Torridonian Sandstone (northwest Scotland): applications
594 for relative dating and implications for warm and cold climate weathering rates. *Boreas* DOI 10.1111/j.1502-
595 3885.2009.00131.
- 596 Kolb, T., Fuchs, M. 2018. Luminescence dating of pre-Eemian (pre-MIS 5e) fluvial terraces in Northern Bavaria (Germany)
597 – Benefits and limitations of applying a pIRIR225-approach. *Geomorphology*, 321, 16-32.
- 598 Laskaris, N., Liritzis, I. 2011. A new mathematical approximation of sunlight penetrations in rocks for surface luminescence
599 dating. *Journal of Luminescence*, 131, 1874-1884.
- 600 Lehmann, B., Valla, P.G., King, G.E., Herman, F. 2018. Investigation of OSL surface exposure dating to reconstruct post-
601 LIA glacier fluctuations in the French Alps (Mer de Glace, Mont Blanc massif). *Quaternary Geochronology*, 44, 63-74.
- 602 Lehmann, B., Herman, F., Valla, P.G., King, G.E., Biswas, R.H. 2019a. Evaluating post-glacial bedrock erosion and surface
603 exposure duration by coupling in situ optically stimulated luminescence and ¹⁰Be dating. *Earth Surface Dynamics*, 7,
604 633-662.
- 605 Lehmann, B., Herman, F., Valla, P.G., King, G.E., Biswas, R.H., Ivy-Ochs, S., Steinemann, O., Christl, M. 2019b.
606 Postglacial erosion of bedrock surfaces and deglaciation timing: New insights from the Mont Blanc massif (western
607 Alps). *Geology*, <https://doi.org/10.1130/G46585.1>
- 608 Li, B., Li, S-H. 2011. Luminescence dating of K-feldspar from sediments: A protocol without anomalous fading correction.
609 *Quaternary Geochronology*. 6, 468-479.
- 610 Liu, J., Murray, A., Sohbaty, R., Jain, M. 2016. The effect of test dose and first IR Stimulation temperature on post-IR IRSL
611 measurements of rock slices. *Geochronometria*, 43, 179-187.
- 612 Luo, M., Chen, J., Liu, J., Qin, J., Owen, L., Han, F., Yang, H., Wang, H., Zhang, B., Yin, J., Li, Y. 2018. A test of rock
613 surface luminescence dating using glaciofluvial boulders from the Chinese Pamir. *Radiation Measurements*, 120, 290-
614 297.
- 615 Merrill, G.P. 1906. *A Treatise on Rocks. Rock-Weathering and Soils*, Macmillan, New York. 400 pp.
- 616 Met Office, 2021. UK Climate averages (1981-2010): Kinlochewe Met station (57.613°N, -5.308°W)
617 <https://www.metoffice.gov.uk/research/climate/maps-and-data/uk-climate-averages/gfhpz0nu4> [Accessed 18/01/2021].

618 Meyer, M.C., Gliganic, L.A., Jain, M., Schmidmair, D. 2018. Lithological controls on light penetration into rock surfaces –
619 Implications for OSL and IRSL surface exposure dating. *Radiation Measurements*, 120, 298-304.

620 Ou, X.J., Roberts, H.M., Duller, G.A.T., Gunn, M.D., Perkins, W.T. 2018. Attenuation of light in different rock types and
621 implications for rock surface luminescence dating. *Radiation Measurements*, 120, 305-311.

622 Parish, R. 1994. The influence of feldspar weathering on luminescence signals and the implications for luminescence dating
623 of sediments. In Robinson, D.A. and Williams, R.B.G., editors, *Rock weathering and landform
624 evolution*, Chichester: Wiley.

625 Pederson, J.L., Chapot, M.S., Simms, S.R., Sohbaty, R., Rittenour, T.M., Murray, A.S., Cox, G. 2014. Age of Barrier
626 Canyon-style rock art constrained by cross-cutting relations and luminescence dating techniques. *PNAS* 111, 12986-
627 12991.

628 Polikreti, K., Michael, C.T., Maniatis, Y., 2002. Authenticating marble sculpture with thermoluminescence. *Ancient TL* 20,
629 11-18.

630 Polikreti, K. Michael, C.T. and Maniatis, Y. 2003. Thermoluminescence characteristics of marble and dating of freshly
631 excavated marble objects. *Radiation Measurements*, 37, 87-94.

632 Portenga, E.W., Bierman, P.R. 2011. Understanding Earth's eroding surface with ¹⁰Be. *GSA Today*, 21, 4-10.

633 Prescott, J.R., Hutton, J.T. 1994. Cosmic ray and gamma ray dosimetry for TL and ESR. *Nuclear Tracks and Radiation
634 Measurements*, 14, 223-227.

635 Reiners, P.W., Brandon, M.T. 2006. Using thermochronology to understand orogenic erosion. *Annual Review of Earth
636 Planetary Science*, doi: 10.1146/annurev.earth.34.031405.125202.

637 Riebe CS, Kirchner JW, Finkel RC. 2003. Long-term rates of weathering and physical erosion from cosmogenic nuclides
638 and geochemical mass balance. *Geochim. Cosmochim. Acta*, 67, 4411-27

639 Roberts, H.M. 2012. Testing Post-IR IRSL protocols for minimising fading in feldspars, using Alaskan loess with
640 independent chronological control. *Radiation Measurements*, 47, 716-724.

641 Robinson, D.A., Williams, R.B.G. 1987. Surface crusting of sandstones in southern England and northern France. In:
642 Gardner, V. (Ed.), *International Geomorphology 1986*, vol. 2. Wiley, Chichester, pp. 623-635.

643 Singhvi, A.K., Deraniyagala, S.U., Sengupta, D. 1986. Thermoluminescence dating of Quaternary red-sand beds: a case
644 study of coastal dunes in Sri Lanka. *Earth and Planetary Science Letters*, 80, 139-144.

645 Sissons, J.B. 1975. A fossil rock glacier in Wester Ross. *Scottish Journal of Geology*, 11, 83-86.

646 Sissons, J.B. 1976. A fossil rock glacier in Wester Ross. Reply to W.B. Whalley. *Scottish Journal of Geology*, 12, 178-79.

647 Smedley, R.K., Duller, G.A.T., Roberts, H.M. 2015. Assessing the bleaching potential of the post-IR IRSL signal for
648 individual K-feldspar grains: implications for single-grain dating. *Radiation Measurements*, 79, 33 – 42.

649 Smedley, R.K., Glasser, N.F., Duller, G.A.T. 2016. Luminescence dating of glacial advances at Lago Buenos Aires (~46 °S),
650 Patagonia. *Quaternary Science Reviews*, 134, 59 – 73.

651 Sohbaty, R., Murray, A.S., Jain, M., Buylaert, J.P., Thomsen, K.J. 2011. Investigating the resetting of OSL signals in rock
652 surfaces. *Geochronometria*, 38, 249-258.

653 Sohbaty, R., Murray, A.S., Buylaert, J.P., Almeida, N.A.C., Cunha, P.P. 2012a. Optically stimulated luminescence (OSL)
654 dating of quartzite cobbles from the Tapada do Montinho archaeological site (east-central Portugal). *Boreas*, 41, 452-
655 462.

656 Sohbaty, R., Murray, A.S., Chapot, M.S., Jain, M., Pederson, J., 2012b. Optically stimulated luminescence (OSL) as a
657 chronometer for surface exposure dating. *Journal of Geophysical Research Solid Earth*, 117.

658 Sohbaty, R., Liu, J., Jain, M., Murray, A.S., Egholm, D., Pairs, R., Guralnick, B. 2018. Centennial- to millennial-scale hard
659 rock erosion rates deduced from luminescence-depth profiles. *Earth and Planetary Science Letter*, 493, 218-230.

660 Stewart, A.D. 1982. Late Proterozoic rifting in NW Scotland: the genesis of the 'Torridonian'. *Journal of Geological Society
661 of London*, 139, 413-420.

662 Stewart, A.D. Donnellson, N.C.B. 1992. Geochemistry and provenance of red sandstones in the Upper Proterozoic Torridon
663 Group in Scotland. *Scottish Journal of Geology*, 28, 143-153.

664 Stocker, T.F., D. Qin, G.-K. Plattner, L.V. Alexander, S.K. Allen, N.L. Bindoff, F.-M. Bréon, J.A. Church, U. Cubasch, S.
665 Emori, P. Forster, P. Friedlingstein, N. Gillett, J.M. Gregory, D.L. Hartmann, E. Jansen, B. Kirtman, R. Knutti, K.
666 Krishna Kumar, P. Lemke, J. Marotzke, V. Masson-Delmotte, G.A. Meehl, I.I. Mokhov, S. Piao, V. Ramaswamy, D.
667 Randall, M. Rhein, M. Rojas, C. Sabine, D. Shindell, L.D. Talley, D.G. Vaughan and S.-P. Xie, 2013: Technical Sum-

668 mary. In: Climate Change 2013: The Physical Science Basis. Contribution of Working Group I to the Fifth Assessment
669 Report of the Intergovernmental Panel on Climate Change [Stocker, T.F., D. Qin, G.-K. Plattner, M. Tignor, S.K. Allen,
670 J. Boschung, A. Nauels, Y. Xia, V. Bex and P.M. Midgley (eds.)]. Cambridge University Press, Cambridge, United
671 Kingdom and New York, NY, USA.

672 Swantesson, J.O.H. 1989. Weathering phenomena in a cool temperate climate. Göteborgs University, Naturgeogr. Inst., Guni.
673 Rapport, 28.

674 Swantesson, J.O.H. 1992. Recent microweathering phenomena in Southern and Central Sweden. Permafrost and Periglacial
675 Processes, 3, 275-292.

676 Swantesson, J.O.H., Moses, C.A., Berg, G.E., Jansson, K.M. 2006. Methods for measuring shore platform micro-erosion: a
677 comparison of the micro-erosion meter and laser scanner. Z. Geomorphology, 144, 1–17.

678 Thomsen, K. J., Murray, A. S., Jain, M. and Bøtter-Jensen, L. 2008. Laboratory fading rates of various luminescence signals
679 from feldspar-rich sediment extracts. Radiation Measurements, 43, 1474 –1486.

680 Thomsen, K.J., Murray, A.S., Jain, M. 2011. Stability of IRSL signals from sedimentary K-feldspar samples.
681 Geochronometria, 38, 1-13.

682 Thomsen, K.J., Kook, M., Murray, A.S., Jain, M. 2018. Resolving luminescence in spatial and compositional domains.
683 Radiation Measurements, 15, 260-266.

684 Thorn, C.E., Darmody, R.G., Dixon, J.C., Schlyter, P. 2001. The chemical weathering regime of Kärkevage, arctic-alpine
685 Sweden. Geomorphology, 41, 37–52.

686 Trauerstein, M., Lowick, S.E., Preusser, F., Schlunegger, F. 2014. Small aliquot and single grain IRSL and post-IR IRSL
687 dating of fluvial and alluvial sediments from the Pativilca valley, Peru. Quaternary Geochronology, 22, 163-174.

688 Trudgill, S.T., Viles, H., Inkpen, R.J., Cooke, R.U. 1989. Remeasurement of weathering rates, St. Paul's Cathedral, London.
689 Earth Surface Processes and Landforms, 14, 175–196.

690 Twidale, C.R., 1982. Granite Landforms. Elsevier, Amsterdam. 372 pp.

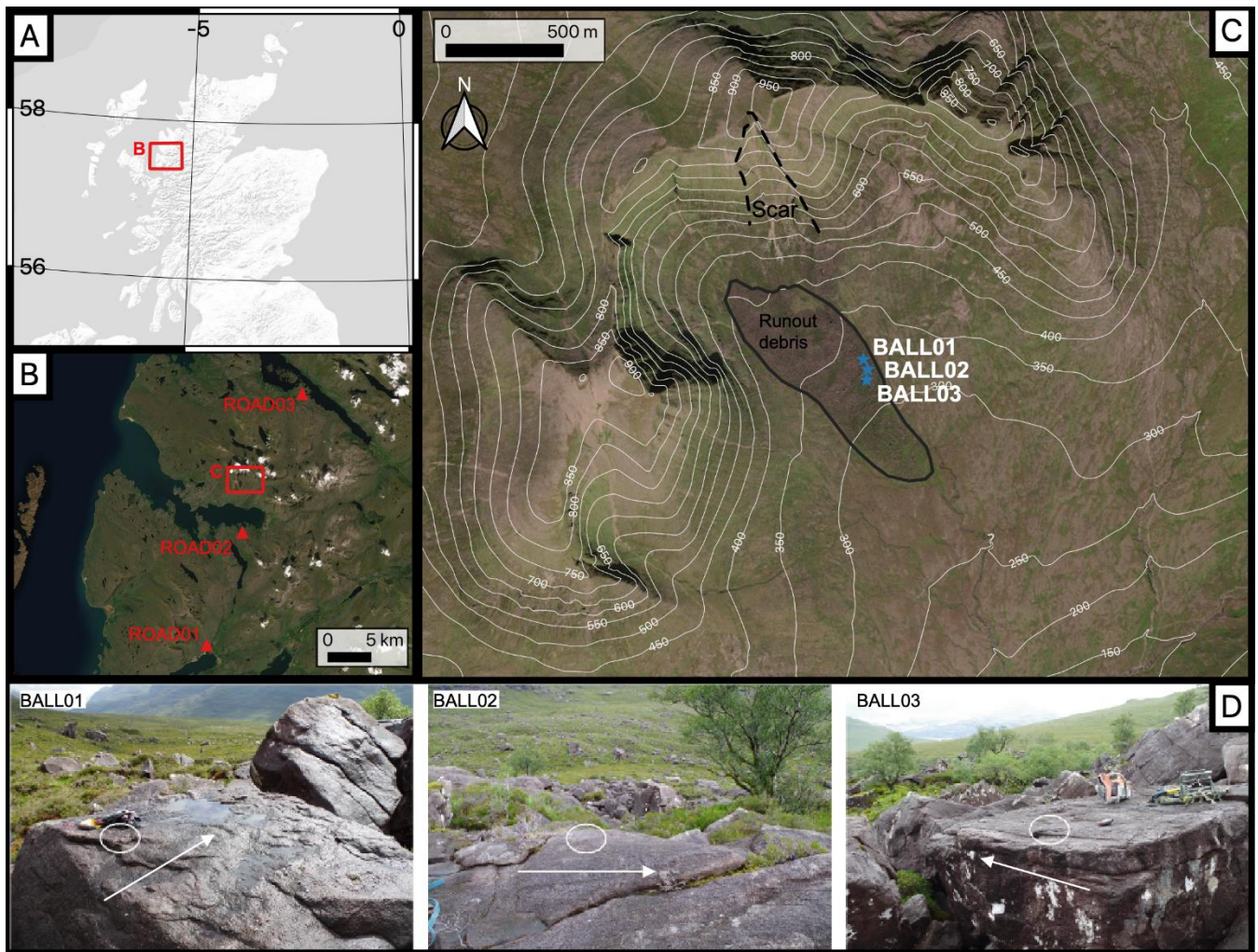
691 Vafiadou, A., Murray, A.S., Liritzis, I., 2007. Optically stimulated luminescence (OSL) dating investigations of rock and
692 underlying soil from three case studies. Journal of Archaeological Science 34, 1659-1669.

693

694

695

696



697
698
699
700
701
702
703
704

Figure 1. Location of the Beinn Alligin rock avalanche (57°35'N, 05°34'W) and roadcut sections in NW Scotland (A,B). Sample sites on the rock avalanche deposit (C). ~~The backgrounds used are ESRI World Terrain Base (A) and ESRI World Imagery (B,C). Contains OS data © Crown copyright and database right (2021).~~ Photographs of flat-topped boulders sampled and the general rock avalanche flow direction (white arrow) for BALL01, BALL02 and BALL03 (D). The backgrounds used are ESRI World Terrain Base (A) and ESRI World Imagery (B,C). Contains OS data © Crown copyright and database right (2021). Scar and runout debris locations mapped in (C) follow Ballantyne and Stone (2004).

A) ROAD01



B) ROAD02



C) ROAD03



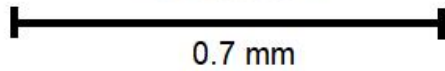
D) BALL01



E) BALL02



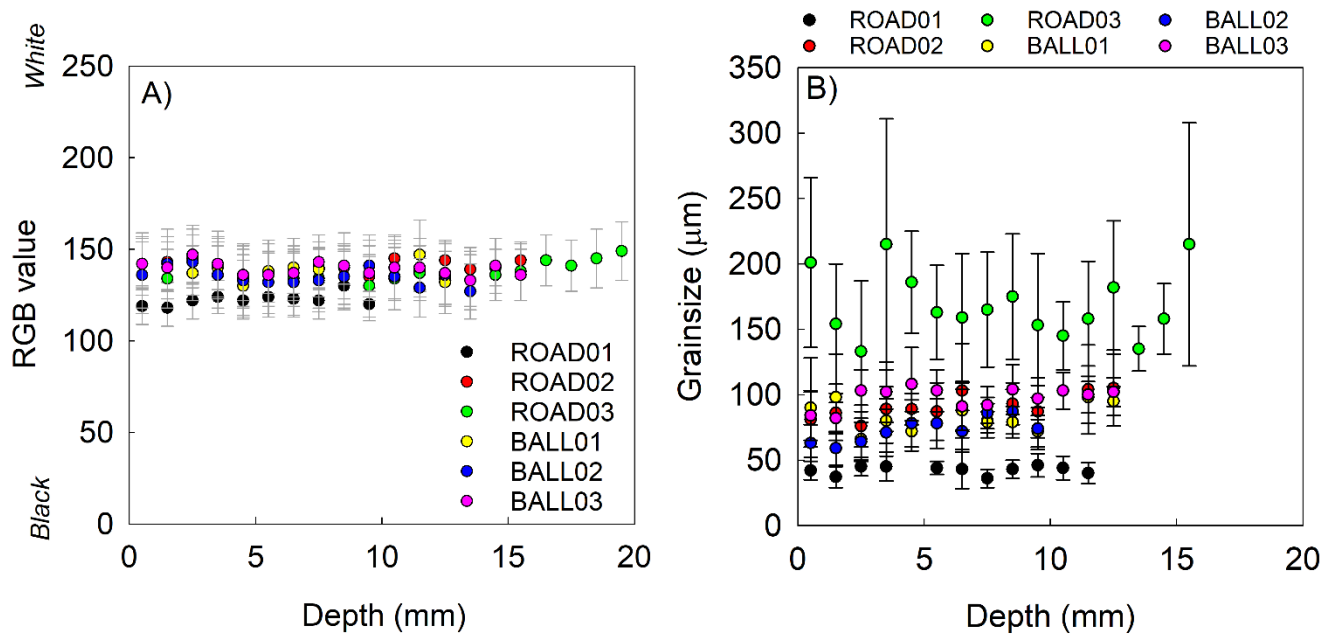
F) BALL03



0.7 mm

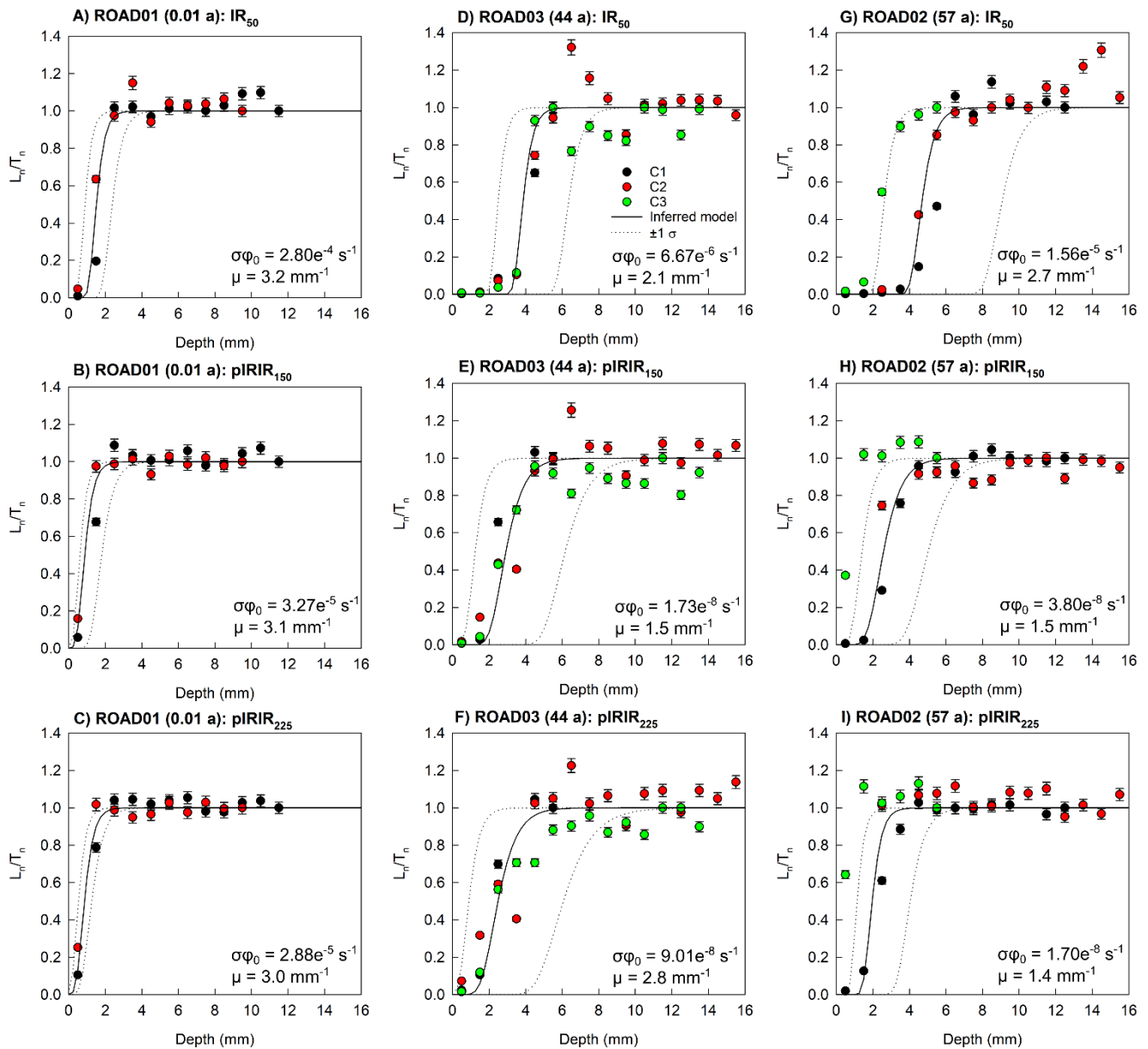
Figure 2. Images of example rock slices (0.7 mm diameter) for each sample taken using the EPSON Expression 11000XL flatbed scanner.

705
706
707

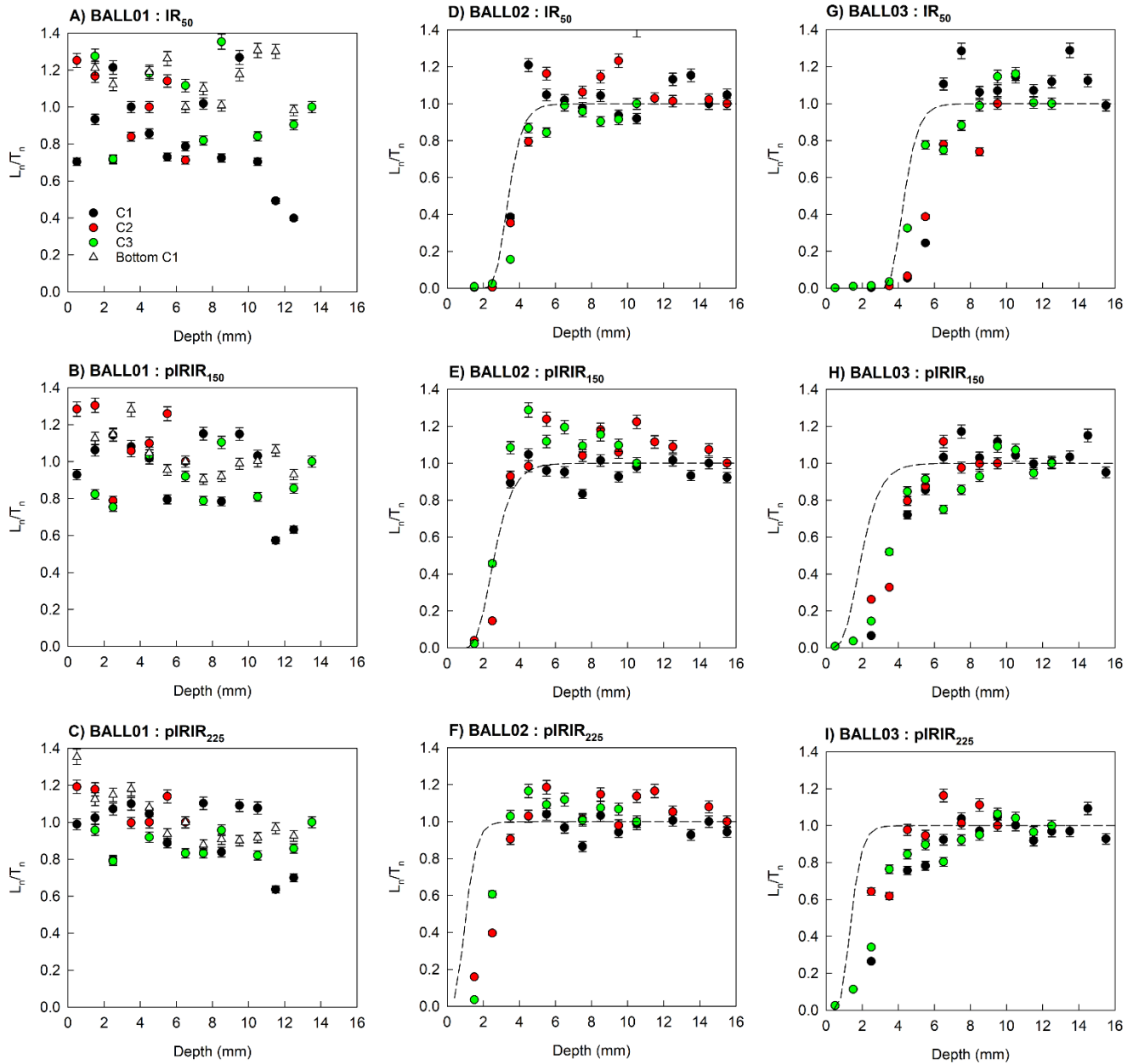


708
709
710
711

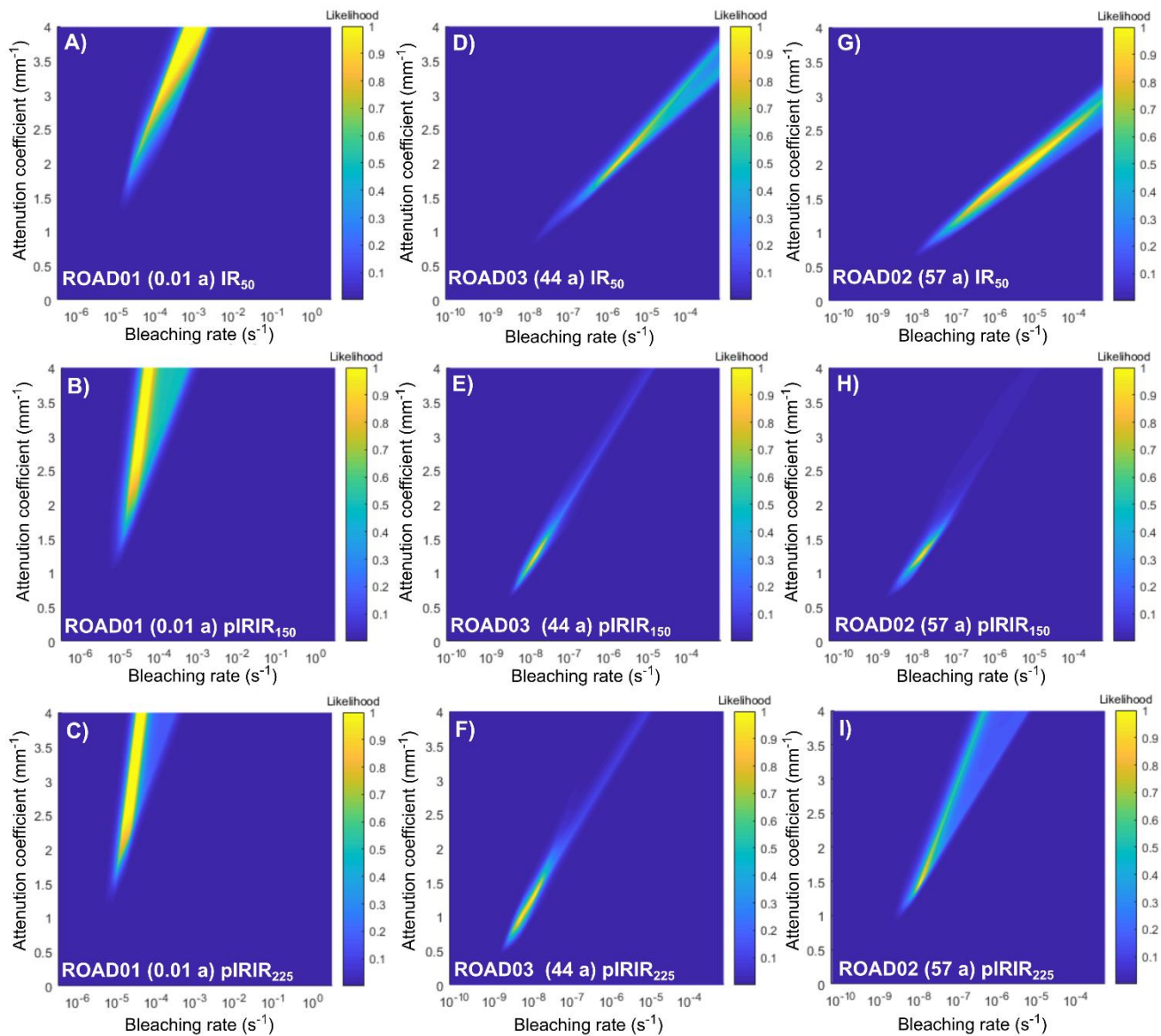
Figure 3. (A) RGB values (0 = black and 255 = white) and (B) grainsize for each sample, calculated as the mean (\pm standard deviation) of the slices at each depth in all of the replicate cores analysed. Note that the RGB values and grainsize measurements were not derived from exactly the same cores, but example cores for each sample.



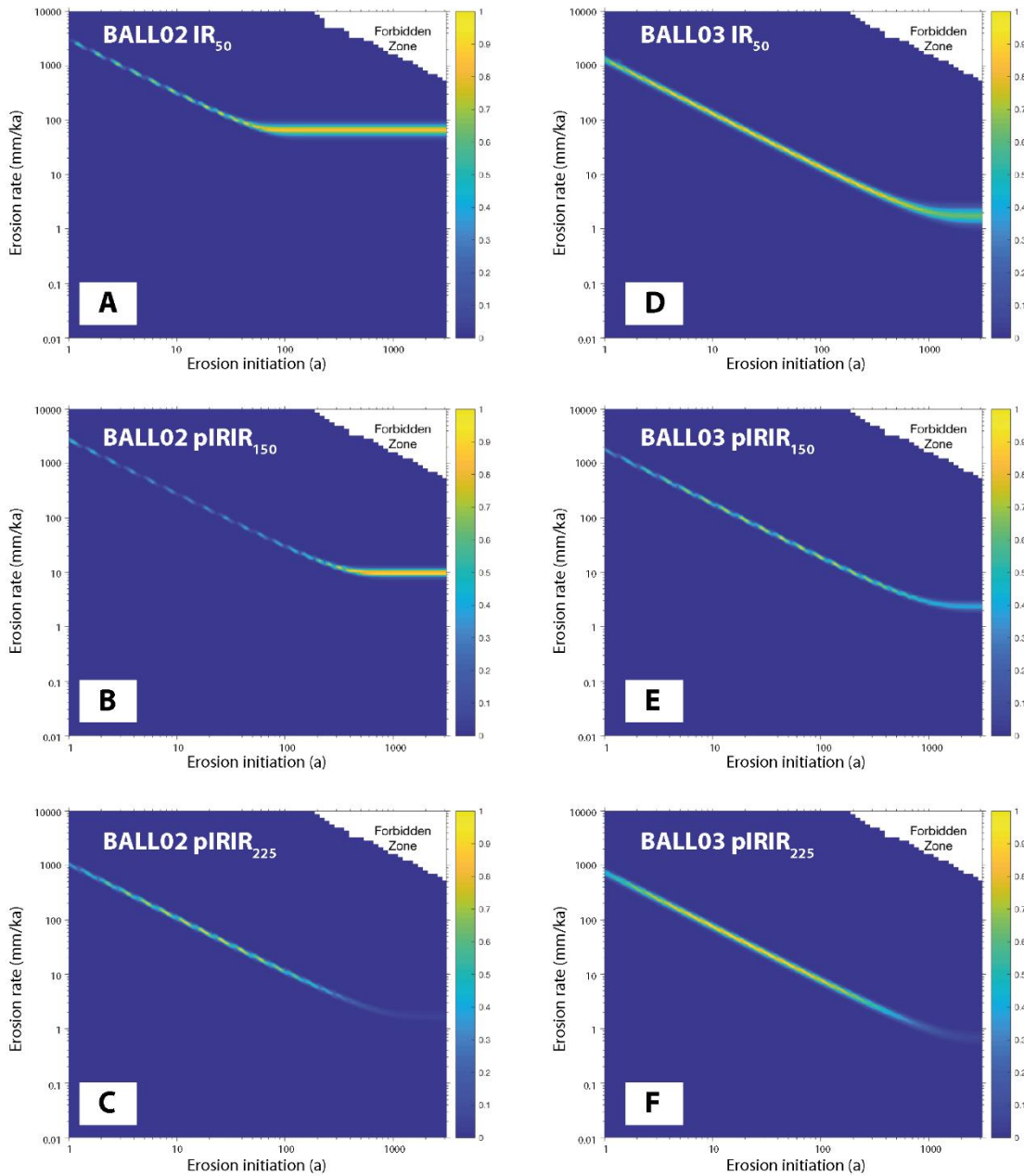
712
713 **Figure 4.** Presented in age-order are the IRSL-depth profiles for each of the three replicate cores analysed per sample using the
714 IR₅₀ (A,D,G), pIRIR₁₅₀ (B,E,H) and pIRIR₂₂₅ (C,F,I) signals for samples ROAD01 (0.01 a; A-C), ROAD03 (44 a; D-F) and
715 ROAD02 (57 a; G-I). All of the raw L_n/T_n data presented in this figure (Table S2-S4) were normalised individually for each core,
716 and subsequent analysis uses the data in this format. The black line shown is the inferred model that was fitted to derive the
717 corresponding $\sigma\phi_0$ and μ values included in each figure. The dotted lines show the corresponding fits modelled using the $\pm 1\sigma$
718 $\sigma\phi_0$ and μ values (Table 2). Note that core 3 of ROAD02 was not considered for fitting.
719



720
721 **Figure 5.** IRSL-depth profiles for each replicate cores analysed using the IR₅₀ (A,D,G), pIRIR₁₅₀ (B,E,H) and pIRIR₂₂₅ (C,F,I)
722 signals for samples BALL01 (A-C), BALL02 (D-F) and BALL03 (G-I). All of the raw L_n/T_n data (Table S5-S7) were normalised
723 individually for each core, and subsequent analysis uses the data in this format. The dashed line is the inferred erosion model for
724 each luminescence depth profile derived from the probability distributions shown in Fig. 7, where erosion rates are included in
725 Table 3.



726
727 **Figure 6.** Presented in age-order is the relationship between $\overline{\sigma\varphi_0}$ and μ parameters for ROAD01 (A-C), ROAD03 (D-F) and
728 ROAD02 (G-I) using the IR₅₀ (A,D,G), pIRIR₁₅₀ (B,E,H) and pIRIR₂₂₅ (C,F,I) signals using the approach of Lehmann et al. (2018).
729
730



731
732
733
734
735

Figure 7. Probability distributions inverted from the respective plots of luminescence depth profiles derived from the inversion results (using the approach of Lehmann et al. 2019a) for samples BALL02 (A-C) and BALL03 (D-F) using the IR₅₀ (A,D), pIRIR₁₅₀ (B,E) and pIRIR₂₂₅ (C,F) signals. Forbidden zones define the range of solutions with high erosion rates and durations that are not feasible within the bounds of the experimental ^{10}Be and luminescence data.

Table 1. Luminescence results for the rock slices analysed in this study. Environmental dose-rates were determined using high-resolution gamma spectrometry. The dose-rates were calculated using the conversion factors of Guerin et al. (2011) and alpha (Bell, 1980) and beta (Guerin et al. 2012) dose-rate attenuation factors. An internal K-content of 10 ± 2 % (Smedley et al. 2012) and internal U and Th concentrations of 0.3 ± 0.1 ppm and 1.7 ± 0.4 ppm (Smedley and Pearce, 2016) were used to determine the internal alpha and beta dose-rates. An a-value of 0.10 ± 0.02 (Balescu and Lamothe, 1993) was used to calculate the alpha dose-rates. Cosmic dose-rates were determined after Prescott and Hutton (1994). Dose-rates were calculated using the Dose Rate and Age Calculator (DRAC; Durcan et al. 2015). Grain size was measured by randomly selecting grains in the rock slices for each sample and calculating ± 1 standard deviation around the mean grain size.

Sample	Grain size (μm)	U (ppm)	Th (ppm)	K (%)	Internal alpha dose- rate (Gy/ka)	Internal beta dose- rate (Gy/ka)	External alpha dose- rate (Gy/ka)	External beta dose- rate (Gy/ka)	External gamma dose-rate (Gy/ka)	External cosmic dose-rate (Gy/ka)	Total dose- rate (Gy/ka)
BALL02	56-91	1.02 \pm 0.15	4.85 \pm 0.28	1.73 \pm 0.29	0.14 \pm 0.04	0.27 \pm 0.06	0.21 \pm 0.05	1.62 \pm 0.00	0.78 \pm 0.08	0.31 \pm 0.03	3.32 \pm 0.12
BALL03	79-117	1.02 \pm 0.14	5.21 \pm 0.28	1.86 \pm 0.29	0.16 \pm 0.04	0.35 \pm 0.08	0.17 \pm 0.04	1.71 \pm 0.00	0.83 \pm 0.08	0.31 \pm 0.03	3.52 \pm 0.12
ROAD01	33-51	2.07 \pm 0.27	7.80 \pm 0.42	2.45 \pm 0.43	0.10 \pm 0.03	0.16 \pm 0.03	0.61 \pm 0.12	2.43 \pm 0.00	1.22 \pm 0.11	0.30 \pm 0.03	4.81 \pm 0.18
ROAD02	67-113	1.55 \pm 0.18	5.67 \pm 0.38	2.88 \pm 0.40	0.15 \pm 0.04	0.32 \pm 0.08	0.23 \pm 0.05	2.59 \pm 0.00	1.16 \pm 0.10	0.30 \pm 0.03	4.76 \pm 0.15
ROAD03	112-225	1.93 \pm 0.21	5.30 \pm 0.30	1.96 \pm 0.31	0.18 \pm 0.04	0.58 \pm 0.20	0.14 \pm 0.04	1.85 \pm 0.00	0.96 \pm 0.08	0.29 \pm 0.03	4.00 \pm 0.22

745

750

Table 2. Calibration factors determined by fitting depth profiles. Note that values presented are medians.

Sample	IRSL signal	$\overline{\sigma\varphi_0}$ (s ⁻¹)	Range ± 1 σ (s ⁻¹)	μ (mm ⁻¹)	Range ± 1 σ (mm ⁻¹)
ROAD01	IR ₅₀	2.80e ⁻⁴	8.41e ⁻⁴ – 6.43e ⁻⁵	3.2	2.5 – 3.8
	pIRIR ₁₅₀	3.27e ⁻⁵	1.16e ⁻⁴ – 2.14e ⁻⁵	3.1	2.2 – 3.7
	pIRIR ₂₂₅	2.88e ⁻⁵	3.99e ⁻⁵ – 1.51e ⁻⁵	3.0	2.3 – 3.6
ROAD02	IR ₅₀	6.67e ⁻⁶	1.27e ⁻⁴ – 3.50e ⁻⁷	2.1	1.4 – 2.6
	pIRIR ₁₅₀	1.73e ⁻⁸	9.64e ⁻⁸ – 9.75e ⁻⁹	1.5	1.1 – 2.3
	pIRIR ₂₂₅	9.01e ⁻⁸	5.53e ⁻⁷ – 2.31e ⁻⁸	2.8	1.8 – 3.6
ROAD03	IR ₅₀	1.56e ⁻⁵	1.64e ⁻⁴ – 1.48e ⁻⁶	2.7	2.0 – 3.2
	pIRIR ₁₅₀	3.80e ⁻⁸	4.40e ⁻⁷ – 1.12e ⁻⁸	1.5	1.1 – 2.5
	pIRIR ₂₂₅	1.70e ⁻⁸	1.17e ⁻⁷ – 4.70e ⁻⁹	1.4	0.9 – 2.5

755

760

Table 3. Luminescence exposure ages and erosion rates determined using the approach of Lehmann et al. (2018) and Lehmann et al. (2019a), respectively. The values of $\overline{\sigma\varphi_0}$ and μ were determined from known-age sample ROAD02 (57 a).

Sample	Signal	$\overline{\sigma\varphi_0}$ (s ⁻¹)	μ (mm ⁻¹)	\dot{D} (Gy/ka)	D_0 (Gy)	Exposure age (a)	Steady-state erosion rate (mm/ka)	Min. initiation time (a)	Max. transient erosion rate (mm/ka)	Initiation time (a)	Min. transient erosion rate (mm/ka)	Initiation time (a)
BALL02	IR ₅₀	6.67e-6	2.1	3.32 ± 0.12	500	8 ± 2	66	73	-	-	-	-
	pIRIR ₁₅₀	1.73e-8	1.5	3.32 ± 0.12	350	66 ± 16	9	593	-	-	-	-
	pIRIR ₂₂₅	9.01e-8	2.8	3.32 ± 0.12	350	263 ± 30	-	-	310	4	12	90
BALL03	IR ₅₀	6.67e-6	2.1	3.52 ± 0.12	500	387 ± 103	-	-	460	3	6	231
	pIRIR ₁₅₀	1.73e-8	1.5	3.52 ± 0.12	350	296 ± 54	-	-	100	19	14	137
	pIRIR ₂₂₅	9.01e-8	2.8	3.52 ± 0.12	350	362 ± 49	-	-	180	4	11	73